1	Lactation alters fluid flow and solute transport in maternal skeleton:
2	a multiscale modeling study on the effects of microstructural changes and loading frequency
3	
4	Xiaohan Lai ^{a*} , Rebecca Chung ^b , Yihan Li ^b , Xiaowei Sherry Liu ^b , Liyun Wang ^{c*}
5	
6	^a Division of Life Sciences and Medicine, University of Science and Technology of China, Hefei,
7	China
8	^b McKay Orthopaedic Research Laboratory, Department of Orthopaedic Surgery, Perelman
9	School of Medicine, University of Pennsylvania, Philadelphia, PA, United States
10	^c Department of Mechanical Engineering, University of Delaware, USA
11	
12	
13	*co-corresponding authors
14	Email: laixhan@ustc.edu.cn, lywang@udel.edu
15	
16	Conflict of Interest:
17	The authors declare that they have no conflict of interest.
18	
19	
20	ABSTRACT: The female skeleton undergoes significant material and ultrastructural changes to meet
21	high calcium demands during reproduction and lactation. Through the peri-lacunar/canalicular
22	remodeling (PLR), osteocytes actively resorb surrounding matrix and enlarge their lacunae and
23	canaliculi during lactation, which are quickly reversed after weaning. How these changes alter the

physicochemical environment of osteocytes, the most abundant and primary mechanosensing cells in bone, are not well understood. In this study, we developed a multiscale poroelastic modeling technique to investigate lactation-induced changes in stress, fluid pressurization, fluid flow, and solute transport across multiple length scales (whole bone, porous midshaft cortex, lacunar-canalicular pore system (LCS), and pericellular matrix (PCM) around osteocytes) in murine tibiae subjected to axial compression at 3N peak load (~320µε) at 0.5, 2, or 4 Hz. Based on previously reported skeletal anatomical measurements from lactating and nulliparous mice, our models demonstrated that loading frequency, LCS porosity, and PCM density were major determinants of fluid and solute flows responsible for osteocyte mechanosensing, cell-cell signaling, and metabolism. When loaded at 0.5 Hz, lactation-induced LCS expansion and potential PCM reduction promoted solute transport and osteocyte mechanosensing via primary cilia, but suppressed mechanosensing via fluid shear and/or drag force on the cell membrane. Interestingly, loading at 2 or 4 Hz was found to overcome the mechanosensing deficits observed at 0.5 Hz and these counter effects became more pronounced at 4 Hz and with sparser PCM in the lactating bone. Synergistically, higher loading frequency (2, 4 Hz) and sparser PCM enhanced flow-mediated mechanosensing and diffusion/convection of nutrients and signaling molecules for osteocytes. In summary, lactation-induced structural changes alter the local environment of osteocytes in ways that favor metabolism, mechanosensing, and post-weaning recovery of maternal bone. Thus, osteocytes play a role in balancing the metabolic and mechanical functions of female skeleton during reproduction and lactation.

- 43 **KEYWORDS**: osteocyte; lactation; lacunar-canalicular system (LCS); pericellular matrix (PCM);
- 44 bone fluid flow; mechanosensing

24

25

26

27

28

29

30

31

32

33

34

35

36

37

38

39

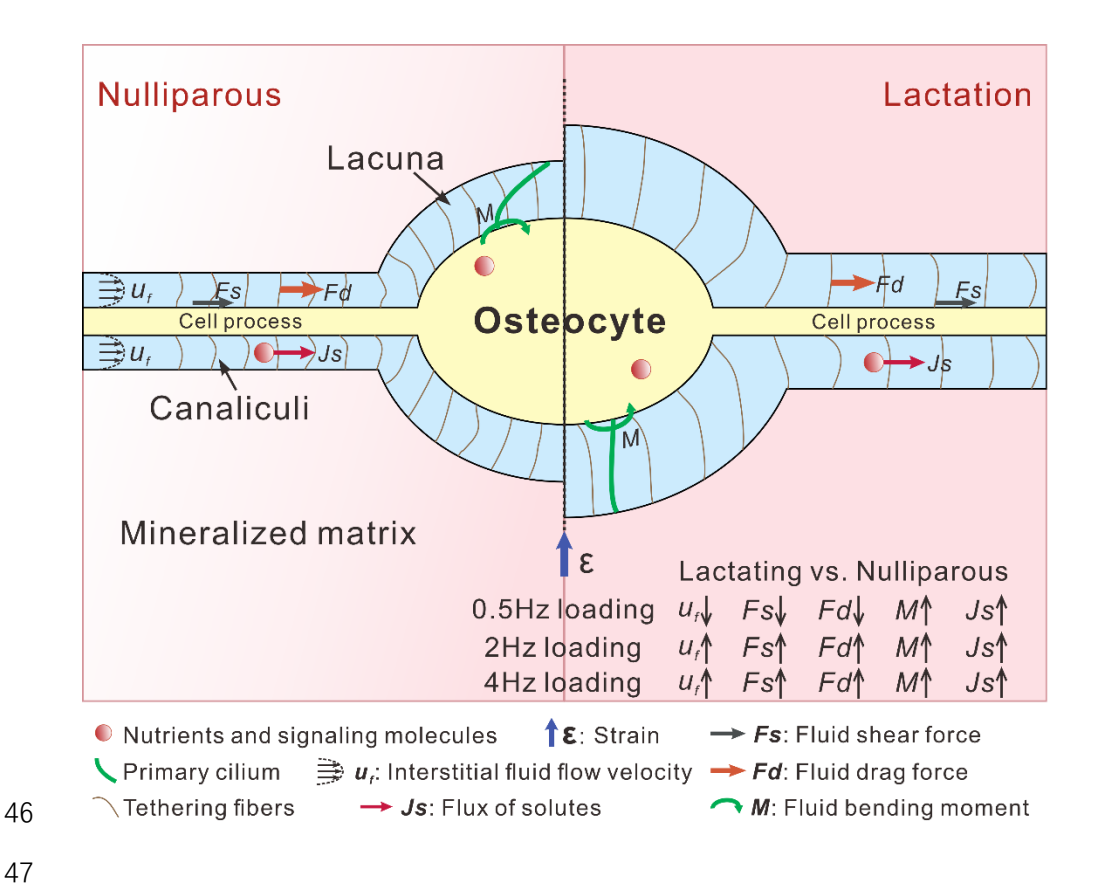
40

41

42

45

GRAPHICAL ABSTRACT



48 Highlights:

- 49 1. Multiscale modeling of lactating and nulliparous murine tibiae under loading
- 2. Loading frequency, LCS porosity, PCM density determine fluid/solute flows in bone
- 3. Lactation causes deficits in osteocyte mechanosensing under 0.5 Hz loading
- 4. Higher frequency (2, 4 Hz) overcomes deficits and enhances transport in lactation
- 5. Osteocytes are important for maintaining female skeletal homeostasis

1. Introduction

54

55

56

57

58

59

60

61

62

63

64

65

66

67

68

69

70

71

72

73

74

75

As early as a century ago, enlargement of osteocytic lacunae was observed in various pathological human ^{1, 2} and animal bones ³, and later referred to as "osteocytic osteolysis" by Belanger ⁴. Although the relevance of osteocytic osteolysis has been debated ^{5, 6}, its critical role in maintaining calcium homeostasis during female reproduction became increasingly accepted 7-10. In the past decade, several studies convincingly demonstrate a robust peri-lacunar/canalicular remodeling (PLR) process during lactation, followed by a quick recovery after weaning 8, 11-14. Intriguingly, lactation offers some surprising benefits such as enhanced sensitivity to mechanical loading ¹⁵ and reduced menopausal bone loss in later life ¹⁶. The structural and material property changes in maternal skeleton have been quantified at the whole bone and tissue levels ¹⁷⁻²², and the osteocyte lacunar and canalicular level 8, 11, 12. Consistently, enlarged lacunae/canaliculi and reduced bone mineral density were found in lactating bone 8, 11, 12, which rapidly returned to basal levels after weaning 12. Activation of the parathyroid hormone receptor 1 (PTHR1) signaling and upregulation of degradation enzymes such as tartrate resistant acid phosphatase (TRAP), cathepsin K, and matrix metalloproteinases in osteocytes have been identified to occur during the PLR process ^{14, 23-25}. What drives the rapid recovery post-lactation, however, remains unclear, although altered fluid/solute transport and osteocyte mechanosensing were proposed to be involved ¹⁰.

Osteocytes are the primary mechanosensing cells in bone ^{7, 26-28} and their surrounding lacunar-canalicular pore system (LCS) serves as the main conduits of interstitial fluid flow, nutrient supply, and cell-cell signaling in bone ²⁹⁻³¹. Upon application of external mechanical loading, the porous bone matrix undergoes solid deformation and fluid pressurization in the LCS pores, driving interstitial fluid flow around osteocytes ²⁷. This loading-induced flow results in shear stress on the

cell process membrane, fluid drag on the transverse tethering elements connecting the cell process with canalicular wall, or bending of primary cilia protruding from the cell body ^{7, 27, 29, 32, 33}. Reduced fluid flow stimulation on osteocytes contributes to diminished anabolic response to mechanical loading in vivo ³⁴. Secondary to fluid flow, these mechanical stimuli can trigger various responses in osteocytes, including elevated intracellular calcium, activated mechanosensitive pathways, and altered release of signaling molecules ³⁵⁻³⁷, including small molecules (e.g., nitric oxide (NO), adenosine triphosphate (ATP), prostaglandin E2 (PGE2)) and larger proteins (e.g., sclerostin, receptor activator for nuclear factor ligand (RANKL), dentine matrix protein 1 (DMP1), osteoprotegerin (OPG)) that act on neighboring osteocytes, as well as surface osteoblasts and osteoclasts ^{7, 26}. To reach their target cells, these molecules pass through the pericellular matrix (PCM) in the LCS via diffusive and/or convective mechanisms ²⁹, and the transport rate is not only dependent on the size and shape of the molecule but also on the sieving property of the LCS ^{38, 39}. Since the LCS structure is a major determinant of fluid and solute flows that are essential for osteocyte function ^{27, 40}, we hypothesize that lactation-induced LCS changes in the maternal skeleton increase the fluid flow-mediated mechanical stimulation of osteocytes and transport of signaling molecules in the LCS, which may contribute to its rapid recovery after lactation.

76

77

78

79

80

81

82

83

84

85

86

87

88

89

90

91

92

93

94

95

96

97

The objective of the present study was to quantify and compare load-induced fluid flow, flow-mediated mechanical stimulation of osteocytes, and solute transport in lactating and nulliparous skeletons using a multiscale modeling approach. We derived key LCS features based on experimental data published in previous literatures and developed customized models of lactating and nulliparous murine tibiae. The model outputs include the stress field at the whole-bone level, pore fluid pressurization at the tissue level, and fluid-solid interactions at the cellular level. The

quantitative analysis provides critical insight for a better understanding of the potential drivers of maternal skeleton adaptation during and after lactation.

2. Methods

98

99

100

101

102

103

104

105

106

107

108

109

110

111

112

113

114

115

116

117

118

119

2.1. The Multiscale modeling framework, model parameters, and fluid flow calculation

We have developed a hierarchical model of a murine tibia under cyclic axial loading (Fig. 1), which has been described in our previous publications ^{38,40} and is summarized herein. In this model, the murine tibia is axially compressed with cyclical loading through its proximal and distal ends (Fig. 1A). The loading is set to be 3 N (~320µɛ at the anteromedial surface of the midshaft) ³⁸ at either 0.5, 2, or 4 Hz ^{41, 42} (Fig. 1A, Table 1). The loading magnitude was chosen because previous fluid flow and solute transport experiments were performed under a peak load of 3 N ⁴³. The results could be scaled linearly to other loading magnitudes for frequency domains less than 5 Hz ³⁵. The three loading frequencies selected are to mimic physiological loading conditions experienced by the tibia during slower (0.5 Hz) and faster (2, 4 Hz) locomotion. The midshaft is idealized as a hollow cylinder bounded by endosteum (radius r_i) and periosteum (radius r_o), with an offset distance L from the long axis of the whole bone (Fig. 1A) 40 . The normal stress distribution at the midshaft cross-section under dynamic compression and bending can be readily obtained using beam theory 40 (Fig. 1A). Our region of interest (ROI) is the LCS located at 30 µm below the medial surface, which is also the ROI in previous in situ imaging studies due to easy access ^{34, 38,} ⁴⁴ (Fig. 1A). The dynamic stress induces fluid pressurization in the porous bone tissue that contains the interconnected LCS channels (n = 74 canaliculi per lacuna, Fig. 1B, Table 1). The hierarchical LCS structure determines the hydraulic resistance to fluid flow ²⁷ and the mathematical formula (Eqs. A1-A6) are detailed in Supplemental Materials. At the ultrastructural level, the pericellular

matrix (PCM) that fills the fluid space between the cell membrane and the mineralized wall provides major hydraulic resistance (Fig. 1C), where the PCM permeability k_p increases with larger fiber spacing Δ , *i.e.*, lower fiber volume fraction kvf (Supplemental Materials, Eqs. A1-A3). At the tissue-level, permeability k is scaled with the average porosity of the LCS that varies with the canalicular annular fluid gap and the number of canaliculi emanating from the lacuna (Supplemental Materials, Eqs. A4-A6) 40. The fluid pore pressure in the bone tissue is driven by the dynamic loading according to Biot theory (Supplemental Materials, Eqs. A8-10) ^{27, 45}. Under the boundary conditions of zero pressure at the endosteum and no leakage at periosteum (Supplemental Materials, Eq. A11), the fluid pressure, pressure gradients, and Darcy's flow velocities in both circumferential and radial directions are obtained (Supplemental Materials, Eqs. A12-20). Detailed spatial velocity profile of the canalicular fluid flow is calculated using the Brinkman equation (Supplemental Materials, Eq. A21) ^{27, 45}. Since our ROI is close to the impermeable periosteum, radial fluid flow is negligible 40 and all the subsequent calculations are based on flow in the circumferential oriented canaliculi (\sim 22% of total canaliculi, n = 16 ⁴⁴, Table 1). The flows in individual canaliculi merge within the lacunar fluid space, where the flow velocity is scaled inversely with the size of the fluid conduit owing to the principle of mass conservation. The spatial profile of the velocity across the lacunar fluid gap is obtained similarly using the Brinkman equation (Supplemental Materials, Eq. A21). The multiscale modeling is mechanically coupled: the mechanical stress field at ROI is a result of the external force applied at the whole bone and serves as input for the tissue-level poroelasticity modeling. Subsequently, the pore pressure and pressure gradients obtained from the tissue-level modeling are inputs to the fluid/solute flow modeling at the LCS level (Figure 1). Thus, this multiscale modeling framework

120

121

122

123

124

125

126

127

128

129

130

131

132

133

134

135

136

137

138

139

140

integrates the mechanical stress, fluid pressure, and velocity profile from the whole bone level (in mm) to the LCS level (in μ m), and to the PCM level (in nm).

142

143

144

145

146

147

148

149

150

151

152

153

154

155

156

157

158

159

160

161

162

163

Two sets of modeling conditions are adopted to simulate fluid flow and solute transport in the nulliparous and lactating female murine skeleton, respectively (Fig. 1C and Table 1). At the whole bone level, it is assumed that the bone size, curvature, and bending rigidity for the two conditions remain the same values as in our previous study 40 because of the minimal changes on cortical bone induced by lactation ¹⁰. At the bone tissue level, the lacunar/osteocyte size (major and minor radii), canalicular/cell process radii, canalicular length and total canalicular number per lacuna, and fluid gaps in the lacuna and canaliculi for the nulliparous case are derived from previous studies of confocal and electron microscopy imaging on 4-5 month old mice 46, 47 (Table 1). Parameters of the osteocyte cell body and processes and the number and spatial distribution of canaliculi emanating from the lacuna are assumed unchanged in the lactating bone, due to the relatively short duration of lactation in rodents (~3 weeks). However, lactation-induced enlargement of the crosssectional area of the lacunae and canaliculi (12.87%, 15%) reported by Qing et al. (2012) 8 and Kaya et al. (2017) 12 are taken into account in the lactating model parameters, including the 6.24% and 7.24% increase in the radii of the lacunar and canalicular walls and the resultant larger fluid gaps and fluid cross-sectional areas (Table 1). At the ultrastructural PCM level, the tethering fibers are assumed to be 2 nm in radius for both lactating and nulliparous conditions, which is based on measurements of perlecan ⁴⁸, a main component of the PCM around osteocytes ⁴⁹. The fiber volume fraction (kvf = 0.061) and the fiber spacing of the PCM (10.35 nm) for the nulliparous case are based on measurements of sieving properties of the osteocytic PCM in young adult mice of 4-5month old ³⁴. Although there have not been any published reports on the PCM changes around

osteocytes in lactating bone, lactation induces an upregulation of matrix degradation enzymes in osteocytes during the PLR process ^{23, 25, 50, 51}, which may lead to degradation of the proteoglycan-containing PCM around osteocyte cell processes ³⁴. While the extent of PCM degradation remains to be determined, we parametrically vary the PCM to be 50%, 75% or 100% of the original fiber volume fraction (termed as 50%kvf, 75%kvf, 100%kvf, respectively) in the lactation model to explore the influence of PCM density reduction. The reduction in the PCM density leads to increased hydraulic permeability at the PCM- and tissue-levels in the lactating bone model (Table 1). Under both conditions, the PCM sieving properties, fiber volume fraction, and fiber spacing in the lacuna are modeled to be the same as those in canaliculi. Within the lacunar fluid space, the primary cilium protruding from the cell body, a mechanosensing apparatus ³², is modeled as an elastic rod of 2 µm in length and 200 nm in diameter ⁵². Osteocyte body is assumed to remain the same in nulliparous or lactating bone. Parameters for the two sets of modeling conditions are summarized in Table 1.

Whole bone level f(t) Axis with constant stress f(t)f(t)Axis with constant stress S cross-sectional view В Tissue level BC: no flow Periosteum Pore pressure p Gradient ∂b/(r∂θ) σ_{z} Lacuna Canalio Endosteum BC: P = 0; free flow Lacunar-canalicular level a-a Cross-sectional views Lacuna Lacuna b-b' gradient $\partial p/(r\partial\theta)$ fs Osteocyte Osteocyte Canalicular wall Canaliculi LCS Expansion in Lactation Mineralized matrix

FIGURE 1. The multiscale model consists of a three-tiered hierarchy including the whole bone level (A), the porous tissue level (B), and the lacunar-canalicular level (C). (A) A murine tibia is subjected to a dynamic loading f(t). The tibial midshaft, idealized as a hollow cylinder, is loaded with f(t) applied at an offset distance L and the resulting normal stress is calculated using beam theory. (B) A schematic of the porous bone tissue containing extensive lacunar-canalicular pore system (LCS). The dynamic stress deforms the bone tissue and pressurizes the fluid pore pressure according to the Biot poroelasticity theory. The tissue-level permeability k is estimated from the anatomical features of the LCS, assuming a regular array of osteocytes and homogenous canalicular distribution. (C) Fluid flow in the LCS fluid space filled with pericellular matrix (PCM) fibers interacts with the cell membrane, tethering fibers, primary cilium, and provides mechanical stimulations acting on the cell process and cell body. Longitudinal (left) and cross-sectional views (right) of the osteocyte LCS (schematics not drawn to scale). Note: the model incorporates numerous canaliculi and dendrites (n = 74) emanating from the osteocyte body. For illustration purposes, only two canaliculi are shown in this schematic. Lacunar and canalicular walls are expanded in lactating vs. nulliparous bone. This multiscale model couples mechanical stress, fluid pressure, and fluid flow driven by pressure gradients from the whole bone level (in mm) to the LCS level (in µm), and to the PCM level (in nm).

→ fs(Fs): Fluid shear force

M: Fluid bending moment

→ u.: Interstitial fluid flow velocity

→ fd(Fd): Fluid drag force

177

178179

180

181

182

183

184

185

186

187

188

189

190 191

192

193

194

\ Tethering fibers

Primary cilium

Table 1. Parameters in the multiscale fluid flow models of nulliparous and lactating bones

	Parameters	Nulliparous		Lactation			
Loading	Peak force (N)/normal stress (MPa) 38, 40, 43	3/4.4					
parameters	Frequency (Hz) ^{38, 40, 43}	0.5; 2; 4					
Whole bone level	Off-center distance of loading (mm) 40		1.5	52			
(murine tibial	Cortical bone periosteum radius (mm) 40		71				
midshaft)	Cortical bone endosteum radius (mm) 40		0.3	27			
Osteocytic	Lacunar radii (R _{major} /R _{minor})(μm) ^{8, 12, 46, 53}	7.900/.	3.900	8.393	/4.143		
lacunar level	Lacunar volume (µm³)	503.3	320	603	.442		
	Osteocyte body radii (r _{major} /r _{minor})(μm) ^{46, 53}	7.410/3.410					
	Osteocyte volume (µm³)		360.	924			
	Lacunar fluid gap η (μm)	0.49	90	0.7	0.733		
	Lacunar fluid cross-sectional area (µm²)	9.0	12	14.448			
Osteocytic	Cell process radius (nm) ⁵³	69.116					
canalicular level	Canalicular/cell process length (µm) 43	30					
	Canalicular wall radius (nm) 12,53	150.3	371	161	161.258		
	Canalicular annular gap (nm)	81.2	.55	92.142			
	Total # of canaliculi per lacuna 53	74					
	# of circumferential canaliculi per lacuna 44	16					
	Canalicular fluid cross-sectional area	0.44	18	0.533			
	(circumferential direction) (μm²)	0.4	TO				
		Nullipa-		Lactation	tation		
		rous	50%kvf	75%kvf	100%kvf		
Pericellular	PCM fiber radius (nm) ⁴⁸	2					
matrix (PCM)	Fiber volume fraction kvf ³⁴	0.061	0.031	0.046	0.061		
level	Fiber edge-to-edge spacing (nm) ³⁴	10.35	16.30	12.57	10.35		
Permeability	k_p : permeability of PCM (nm ²) ^{27, 45}	13.94	40.67	22.05	13.94		
	k: the tissue-level permeability (nm ²) ^{27, 45}	0.010	0.032	0.018	0.012		

2.2. Flow-mediated stimulations on osteocytes and their cell processes

The multiscale models of nulliparous and lactating murine tibiae are subjected to a sinusoidal compression loading scheme with a peak load of 3N at either 0.5, 2 or 4 Hz. Following the procedure outlined above, the canalicular velocity profile can be obtained (Supplemental Materials,

Eq. A21), from which the flow-mediated stimulations at the canalicular level are derived, including shear stress (Eq. A22), shear force on the cell process membrane (Eq. A23) and the drag force on the PCM fibers (Eq. A24) per unit length (μm) of the cell process. Similar outcome measures, which act on the cell body via fluid shear and drag force, are derived at the lacunar level. Furthermore, flow-induced bending moment on primary cilium can be derived for both nulliparous and lactation cases, by first obtaining the distributed drag force on the primary cilium using the solution of a cylinder in low Reynolds number Stokes flow ⁵⁴ and then integrating the bending moment along the entire length of the primary cilium (see Eqs. B1-B4 in Supplemental Materials).

2.3. Sensitivity of flow-mediated stimulations to the LCS structural variations

Although the two sets of model configurations allowed us to compare the flow-mediated stimulations between nulliparous and lactating murine bones with predetermined LCS parameters (Table 1). In reality, the LCS dimension could vary in a wider range, depending on the animal species, age, and location of bones. To understand the sensitivity of those flow-mediated forces to the LCS structural variations, we performed a parametric study, where the mineralized walls outlined the lacunae and their associated canaliculi are assumed to vary between 80% and 140% of the reference nulliparous values, and the loading is 3 N at either 2 or 4 Hz. LCS reduction and expansion have been observed in cases of perlecan deficiency ⁴⁹, and Paget's disease or renal osteodystrophy ^{55, 56}, respectively. These LCS structural variations could affect the overall behavior of the fluid flow and flow-mediated stimulations on osteocytes. Other model parameters were kept the same as listed in Table 1.

2.4. Transport of molecules relevant to the osteocyte function

226

227

228

229

230

231

232

233

234

235

236

237

238

239

240

241

242

243

244

245

246

247

The presence of PCM fibers in the LCS fluid conduits is expected to hinder the transport of various molecules secreted by or acting on osteocytes. This sieving property is quantified by the reflection coefficient σ , which describes the reduction of solute convection relative to the fluid motion owing to the finite size of the solute and the steric exclusion effect from the PCM fibers (i.e., solutes cannot penetrate into PCM fibers). We have derived a close-form mathematical solution for the reflection coefficient of a solute penetrating fiber arrays as a function of the solute radius, the fiber radius (2 nm), and the fiber spacing (or fiber volume fraction) ³⁸. The formula (Eq. C1 in Supplemental Materials) allows us to evaluate how PCM in lactating bone, assumed to be 50%, 75%, or 100% of the basal level in nulliparous bone, affects the velocity and volumetric flux of a particular solute under the specific loading condition (3N at either 0.5, 2, or 4 Hz). The solutes of our interest are the following molecules with molecular weight increasing from 40 to 140,000 Dalton: calcium, glucose, estrogen, PGE2, ATP, Insulin-like growth factor 1 (IGF-1), parathyroid hormone (PTH), sclerostin, soluble RANKL, transforming growth factor beta (TGF-β), tartrateresistant acid phosphatase (TRAP), OPG, DMP-1, Romosozumab (sclerostin antibody) (Table 3). The solute velocity U_s in the lacuna and canaliculi conduits is reduced from the fluid velocity u_f (obtained in the preceding section) by a factor of $(1-\sigma)$, i.e., $U_s = (1-\sigma) \times u_f$.

The solute diffusivity in the LCS of nulliparous and lactating bone is also sensitive to changes in PCM density due to the solute-fiber interactions. Curry and Michel established a fiber matrix model ⁵⁷ to describe the reduced diffusivity (*D*) of a solute (radius r_s) in a random array of fibers (radius r_f) from the free diffusivity in water (D_θ): $\frac{D}{D_\theta} = exp\left(-\sqrt{kvf}\left(1 + \frac{r_s}{r_f}\right)\right)$, which is used to estimate the reduced diffusivity for the solutes of our interest (Table 3). The free diffusivity D_θ is

estimated from the molecular weight (MW) using the Polson method $D_0 = \frac{A}{MW^{(1/3)}}$, A is a constant with value 2.85×10^{-5} cm²·sec⁻¹·g^{1/3}·mol^{-1/3} ^{58, 59}. The hydrodynamic radius (R_a) of a solute can be estimated from the free diffusivity D_0 using the Stokes–Einstein equation: $R_a = \frac{k_B T}{6\pi\mu D_0}$, where k_B is the Boltzmann constant (1.38×10⁻²³ J·K⁻¹), T is room temperature (298 K) and μ is the viscosity of water (1.06×10⁻³ kg·m⁻¹ s⁻¹). Furthermore, the volumetric influx of three representative solutes (ATP, IGF-1, and sclerostin) in the canaliculi can be derived based on the solute velocity and fluid cross-sectional area.

3. Results

3.1. Fluid pressure gradients and fluid flow profiles in lactating vs. nulliparous bone

Load-induced fluid pressure gradient varies with loading frequency and PCM density, which collectively determine the spatial fluid velocity profiles within the lacuna and canaliculi (Fig. 2). Under 3 N (~320 με) axial compression at either 0.5, 2, or 4 Hz (Figs. 2A-2C), the peak values of the radial and circumferential pressure gradients at our region of interest (Fig. 1A) are higher at 2 or 4 Hz than 0.5 Hz (Figs. 2D-2I). Moreover, the circumferential pressure gradients (Figs. 2D-2F) are more than ten times higher than the radial pressure gradients (Figs. 2G-2I), thereby justifying our focus on the circumferential flow in the subsequent calculations. Lactating bone with sparser PCM (50% or 75%kvf) experiences ~50% lower pressure gradients relative to the nulliparous bone under 0.5 Hz loading (Figs. 2D, 2G), while such differences are reduced under 2 Hz loading (Figs. 2E, 2H) and nearly abolished under 4 Hz loading (Figs. 2F, 2I). As expected, increasing the loading frequency from 0.5 to 2 or 4 Hz results in ~2-4 fold increases in the pressure gradients, depending on the PCM density (Figs. 2D-2I). As for the flow velocity profiles resulting from the above peak

circumferential pressure gradients, the magnitude of the canalicular flow is \sim 20 times higher than that of the lacunar flow, regardless of the loading frequency or PCM density (Figs. 2J-2O). Furthermore, the profile of the canalicular flow is closer to that of plug flow while the profile of the lacunar flow is nearly parabolic (Figs. 2J-2O). In lactation, the expansion of fluid gaps alone (92 vs. 81 nm in canaliculi or 490 vs. 733nm in lacuna) flattens the velocity curves with lower peak values (nulliparous vs. Lactation 100%kvf), while the peak velocity is elevated with PCM density decreasing, *i.e.*, the peak fluid velocity is ranked as 50%kvf > 75%kvf > 100%kvf (Figs. 2J-2O). Synergistically, a higher loading frequency (2 or 4 Hz) with sparser PCM density (50% or 75%kvf) leads to higher peak velocities in lactating bone than in nulliparous bone (Figs. 2J-2O).

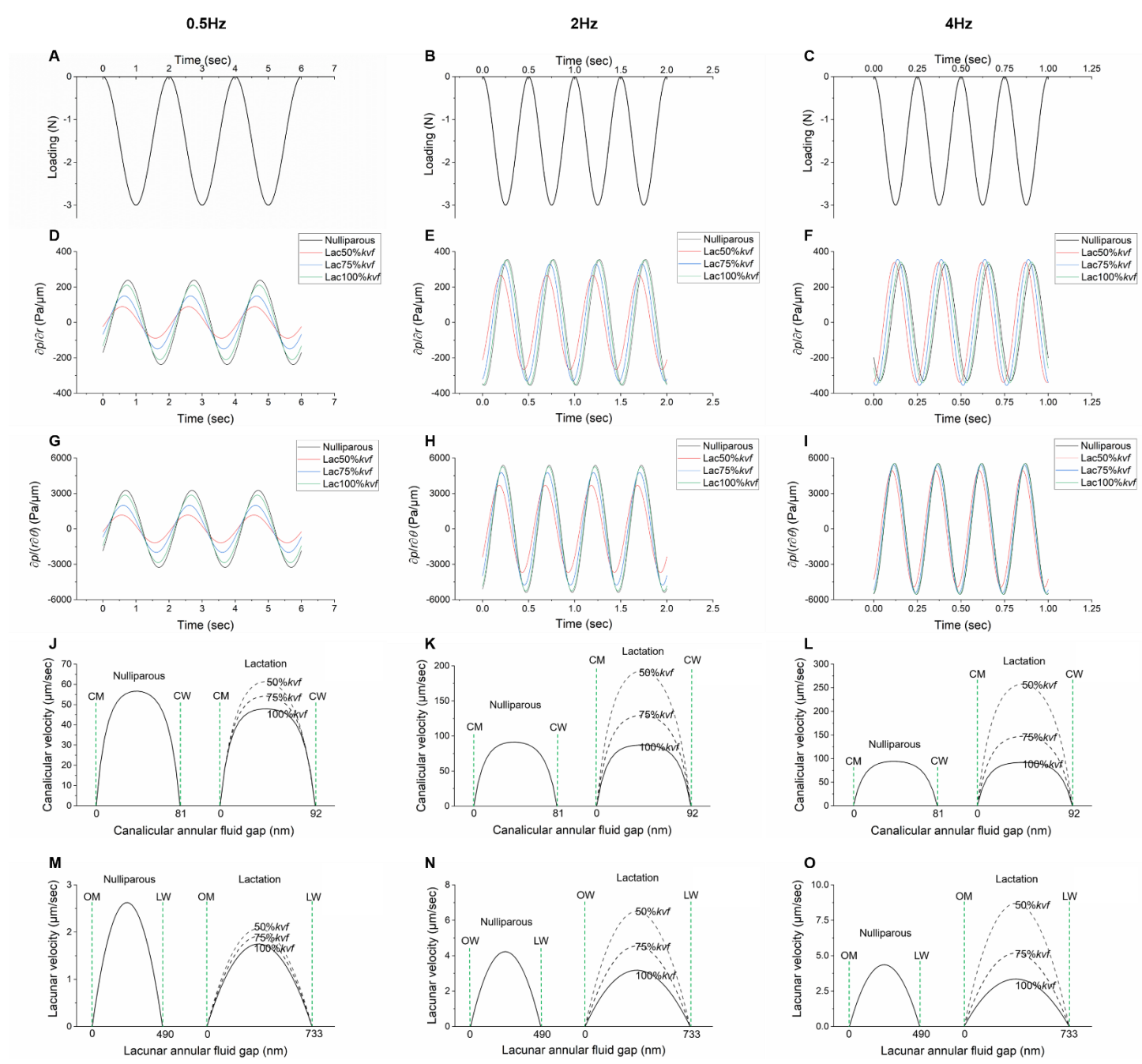


FIGURE 2. Loading induces fluid pressurization and fluid flow in bone. (A-C) Tibiae are dynamically loaded with 3N at 0.5, 2, or 4 Hz. (D-F) Radial pressure gradients and (G-I) circumferential pressure gradients (> 10-fold higher) induced by loading in nulliparous or lactating murine tibial midshaft below periosteum (region of interest shown in Fig. 1A). Circumferential velocity profiles in the canaliculi (J-L) or lacuna (M-O) in nulliparous or lactating tibia. The PCM density of lactating bone is assumed to be 50%, 75%, to 100% of that of nulliparous bone (*kvf*). The width of the canalicular or lacunar annular fluid gap is enlarged in the lactating bone. CM: cell process membrane, CW: canalicular wall, OM: osteocyte body membrane, LW: lacunar wall.

3.2. Flow-mediated mechanical stimulations in lactating vs. nulliparous bone

Relative to the nulliparous bone, flow-mediated shear force and drag force on the osteocyte cell process and cell body in the lactating bone are shown to mostly decrease at 0.5 Hz but begin to increase at 2 or 4 Hz, especially in the cases of sparser PCM. In contrast, the bending moment of the primary cilium increases in the lactating bone regardless of the loading frequency (Table 2). When comparing the lactation 100%kvf case vs. the nulliparous case at the 0.5 Hz loading frequency, the increased LCS dimension alone reduces the mean canalicular fluid velocity by 13.5%, shear stress (force) on cell process by 16.9% (15.4%), the mean lacunar fluid velocity by 35.8%, and shear stress (force) on cell body by 36.4% (36.2%) in lactating bone. Meanwhile, the increased LCS dimension (lactation 100%kvf vs. nulliparous case) increases the bending moment on primary cilium by 43.4% with relatively small change in total force (summation of shear and drag force) along cell process (+0.8%) or cell body (-1.5%) in lactating bone (0.5 Hz, Table 2). For the three assumed PCM density cases in lactation (50%, 75%, or 100%kvf), 26 out of 33 model outputs decrease relative to the nulliparous case (as shown in negative percentages of change) under 0.5 Hz loading (Table 2). Meanwhile, when loading frequency is increased from 0.5 Hz to 2 or 4 Hz, the magnitudes of model outputs increase substantially regardless of nulliparous or lactating status or PCM density (Table 2). Relative to the nulliparous bone, 2 Hz loading of lactating bone induces an increase in 20 out of 33 model outputs, including flow-mediated total force along cell process (+1.6%, +13.6%, +13.9%) and cell body (-7.5%, +8.2%, +11.2%) and bending of primary cilium (+231.8%, +132.0%, +62.1%) for a given PCM density of 50%, 75%, or 100%kvf (2 Hz, Table 2). More model outputs (25 out of 33) are increased in lactating bone under 4 Hz loading relative to nulliparous bone, and specially, the total force along cell process and cell body as well as bending of primary cilium are all increased regardless of PCM density (4

292

293

294

295

296

297

298

299

300

301

302

303

304

305

306

307

308

309

310

311

312

314 Hz, Table 2).

315 316

Table 2. Loading-induced flow-mediated stimulations in lactating vs. nulliparous bones

	Nulliparous	Lactation				
	(reference)	(% change relative to Nulliparous*)				
		50%kvf	75%kvf	100%kvf		
Loading Frequency (Hz)		I	0.5			
Fluid velocity in canaliculi (mean	43.93	45.09	41.54	38.00		
value, μm/sec)		(+2.6%)	(-5.4%)	(-13.5%)		
Shear stress on cell process (Pa)	6.10	4.69	4.93	5.07		
		(-23.1%)	(-19.2%)	(-16.9%)		
Shear force on cell process $(pN/\mu m)$	2.6	2.0	2.1	2.2		
		(-23.1%)	(-19.2%)	(-15.4%)		
Drag force on cell process (pN/μm)	23.0	11.3	17.5	23.6		
		(-50.9%)	(-23.9%)	(+2.6%)		
Total force on cell process (pN/μm)	25.6	13.3	19.6	25.8		
		(-48.0%)	(-23.4%)	(+0.8%)		
Fluid velocity in lacuna (mean	2.18	1.67	1.53	1.40		
value, μm/sec)		(-23.4%)	(-29.8%)	(-35.8%)		
Shear stress on cell body (Pa)	0.22	0.11	0.13	0.14		
		(-50.0%)	(-40.9%)	(-36.4%)		
Shear force on cell body (pN/μm)	4.7	2.3	2.7	3.0		
		(-51.1%)	(-42.6%)	(-36.2%)		
Drag force on cell body (pN/μm)	229.4	109.0	168.8	227.7		
		(-52.5%)	(-26.4%)	(-0.7%)		
Total force on cell body (pN/μm)	234.1	111.3	171.5	230.7		
		(-52.5%)	(-26.7%)	(-1.5%)		
Bending moment on primary cilium	2.05	3.49	3.22	2.94		
(pN.nm)		(+70.2%)	(+57.1%)	(+43.4%)		
Loading Frequency (Hz)			2			
Fluid velocity in canaliculi (mean	70.77	141.54	99.05	69.11		
value, μm/sec)		(+100%)	(+40%)	(-2.3%)		
Shear stress on cell process (Pa)	9.82	14.73	11.75	9.23		
		(+50%)	(+19.7%)	(-6.0%)		
Shear force on cell process (pN/μm)	4.27	6.39	5.10	4.01		
		(+49.6%)	(+19.4%)	(-6.1%)		
Drag force on cell process (pN/μm)	37.01	35.53	41.80	43.02		
		(-4.0%)	(+12.9%)	(+16.2%)		
Total force on cell process (pN/μm)	41.28	41.92	46.9	47.03		
		(+1.6%)	(+13.6%)	(+13.9%)		
Fluid velocity in lacuna (mean	3.52	5.22	3.65	2.55		
value, μm/sec)		(+48.3%)	(+3.7%)	(-27.6%)		

Shear stress on cell body (Pa)	0.36	0.34	0.30	0.25
		(-5.6%)	(-16.7%)	(-30.6%)
Shear force on cell body (pN/μm)	7.62	7.20	6.45	5.44
		(-5.5%)	(-15.4%)	(-28.6%)
Drag force on cell body (pN/μm)	369.76	341.72	401.79	414.03
		(-7.6%)	(+8.7%)	(+12.0%)
Total force on cell body (pN/μm)	377.38	348.92	408.24	419.47
		(-7.5%)	(+8.2%)	(+11.2%)
Bending moment on primary cilium	3.30	10.95	7.66	5.35
(pN.nm)		(+231.8%)	(+132.0%)	(+62.1%)
Loading Frequency (Hz)			4	
Fluid velocity in canaliculi (mean	72.95	189.33	112.72	72.85
value, µm/sec)		(+159.5%)	(+54.5%)	(-0.1%)
Shear stress on cell process (Pa)	10.12	19.70	13.37	9.73
-		(+94.7%)	(+32.1%)	(-3.9%)
Shear force on cell process (pN/μm)	4.4	8.6	5.8	4.2
		(+95.5%)	(+31.8%)	(-4.5%)
Drag force on cell process (pN/μm)	38.2	47.5	47.6	45.4
		(+24.3%)	(+24.6%)	(+18.8%)
Total force on cell process (pN/μm)	42.6	56.1	53.4	49.6
		(+31.7%)	(+25.4%)	(+16.4%)
Fluid velocity in lacuna (mean	3.63	6.98	4.16	2.69
value, µm/sec)		(+92.3%)	(+14.6%)	(-25.9%)
Shear stress on cell body (Pa)	0.37	0.45	0.34	0.27
		(+21.6%)	(-8.1%)	(-27.0%)
Shear force on cell body (pN/μm)	7.9	9.6	7.4	5.7
		(+21.5%)	(-6.3%)	(-27.8%)
Drag force on cell body (pN/μm)	381.3	456.9	457.9	436.8
		(+19.8%)	(+20.1%)	(+14.6%)
Total force on cell body (pN/μm)	389.2	466.5	465.3	442.5
/		(+19.9%)	(+19.6%)	(+13.7%)
Bending moment on primary cilium	3.40	14.64	8.73	5.64
(pN.nm)		(+330.6%)	(+156.8%)	(+65.9%)

Note: * The % values in the parentheses are calculated as [lactation/nulliparous-1]*100 $\,$

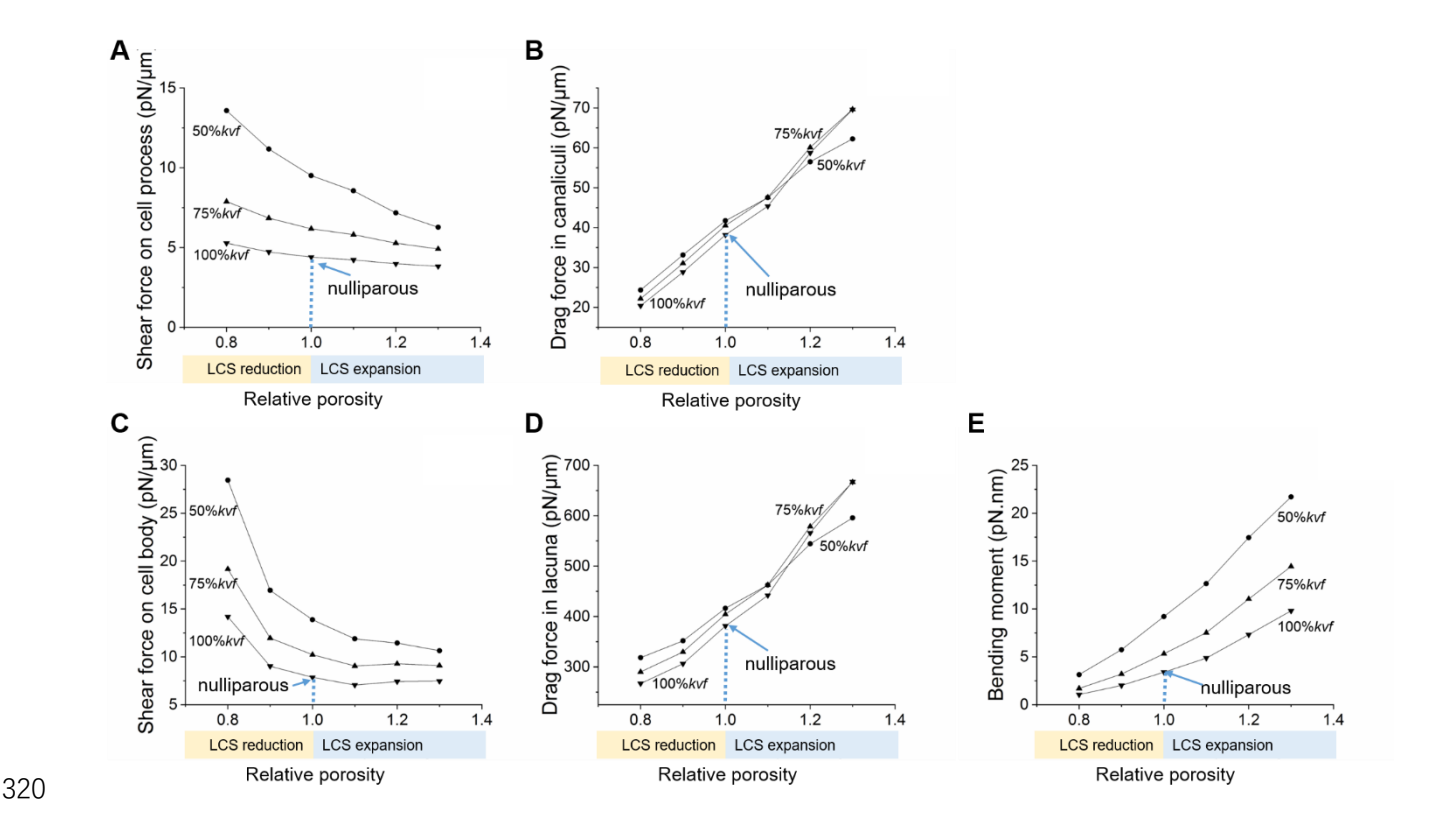


FIGURE 3. Parametric sensitivity study. The variations of LCS porosity and PCM fiber density affect (A) shear force, (B) drag force on the cell process, and (C) shear force, (D) drag force on the cell body, as well as (E) bending moment on the primary cilium protruding from the cell body. The LCS porosity is reduced or expanded, varying from 0.8 to 1.3 with the porosity of nulliparous bone being the reference (1.0). The PCM density is varied at 50%, 75%, and 100% of the basal level in nulliparous bone (kvf = 0.061). Other bone parameters are kept the same as listed in Table 1. The bone is modeled under axial loading at 3N peak load and 4 Hz. The region of interest (30 μ m under the medial surface) is shown in Fig. 1A.

3.3. Sensitivity of flow stimulations to the LCS structure variations

Upon examining a wider range of LCS porosity variations from the reference nulliparous condition, we can observe that shear force on the cell process decreases almost linearly with increasing LCS porosity and its rate of decline is higher with sparser PCM (Fig. 3A). In contrast, the drag force on the cell process increases nearly linearly with increasing LCS porosity and the rate of increase does not differ substantially at various PCM densities (Fig. 3B). In the lacuna, the shear force on the cell body decreases nonlinearly with increasing LCS porosity and the rate of

decline is higher at a smaller LCS and sparser PCM (Fig. 3C). In contrast, the drag force on the cell body increases nearly linearly with the LCS porosity and the rate of increase does not differ substantially at various PCM densities (Fig. 3D). The bending moment of the primary cilium increases nearly linearly with increasing LCS porosity (Fig. 3E). Similar patterns are observed for 2 Hz loading (Supplemental Materials-Figure 1S).

3.4. Solute transport in the LCS of the nulliparous vs. lactating bones

As expected, the reflection coefficient in the PCM-filled LCS increases with molecular weight and the increase is higher with denser PCM (Fig. 4A). The reduced diffusivity in the LCS (*D/D₀*, relative to free diffusion) decreases with increasing molecular weight and the rate of decrease is higher with denser PCM (Fig. 4B). In the case of nulliparous and lactation with 100%*kyf*, solutes relevant to osteocyte function with molecular weight ranging from 40 to 146,000 Dalton would lag behind fluid flow by 0.1% to 48.6% and diffuse at 77% to 48% of their respective free diffusion rates (Table 3). When the PCM density is reduced in lactating bone (75% or 50% *kvf*), these solutes would experience reduced sieving and increased diffusion and the extent of change (relative to 100%*kvf*) is more pronounced for larger solutes (Table 3). For three representative solutes (ATP, IGF-1, and sclerostin), the solute influx into the osteocyte lacuna at the region of interest is clevated in the lactating bone compared to that in the nulliparous bone, and the increase is higher with sparser PCM (50% vs. 75% vs. 100% *kvf*) and amplified at higher loading frequency (2 or 4 vs. 0.5 Hz) (Figs. 4C-4E).

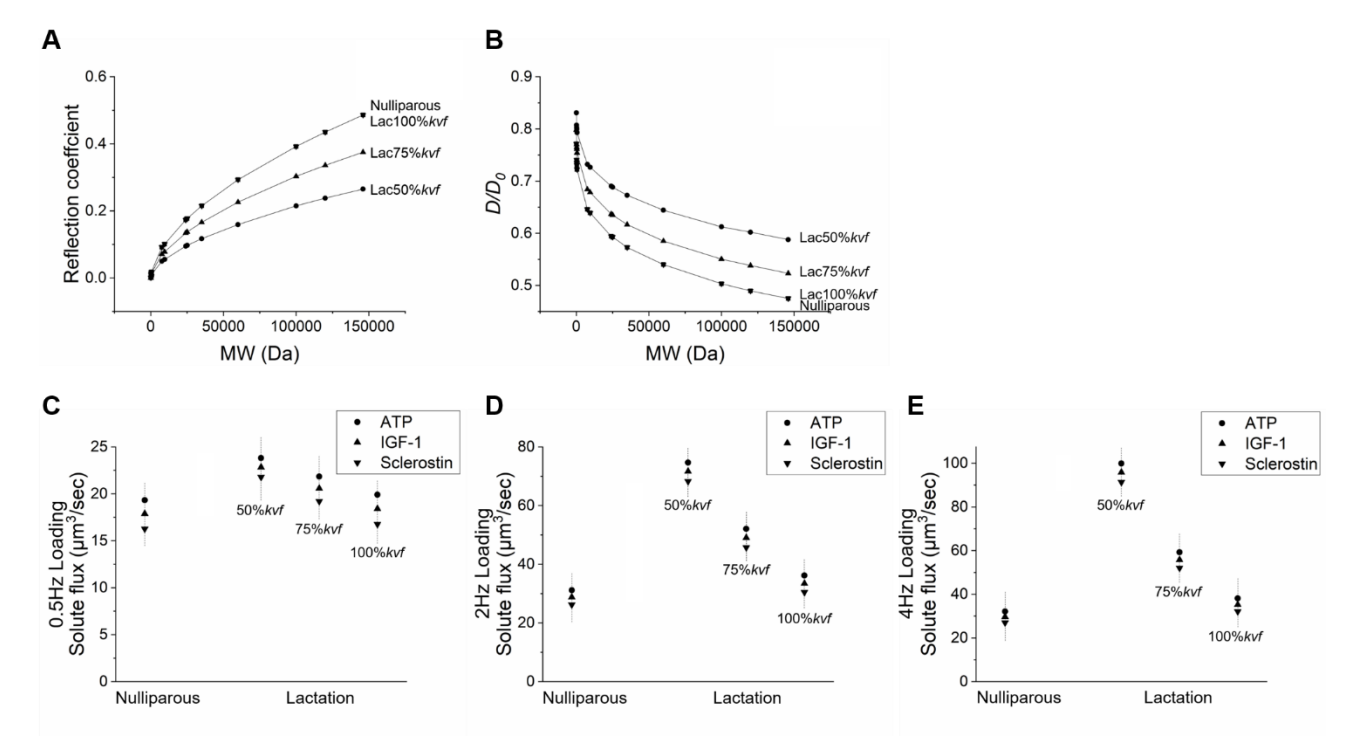


FIGURE 4. The effects of varying PCM density on solute transport. (A) Reflection coefficient and (B) reduced diffusivity (D/D_0) as a function of solute molecular weight for nulliparous or lactating bones with their PCM density being 100%, 75%, or 50%kvf (kvf = 0.061). Total solute influx J_s for three representative molecules (ATP [507 Da], IGF-1 [7600 Da], and sclerostin [24000 Da]) in the nulliparous or lactating bone under cyclical loading of 3N at either (C) 0.5 Hz, (D) 2 Hz, or (E) 4 Hz. (Note the different scales in panel C-E)

Table 3. Effects of PCM density on solute transport in the LCS

Solutes	MW (Da)	Stokes radius (nm)	Free diffusivity D_{θ} (μ m ² /s)	Nulliparous Lactation (100%kvf)		Lactation (75%kvf)		Lactation (50%kvf)	
				Refl. coef	D/D_{θ}	Refl. coef	D/D_{θ}	Refl. coef	D/D_{θ}
Calcium	40	0.103	778	0.001	0.77	0.000	0.80	0.000	0.83
Glucose	180	0.433	504.8	0.009	0.74	0.007	0.77	0.005	0.81
Estrogen	272	0.497	439.7	0.012	0.73	0.009	0.77	0.006	0.80
PGE2	352	0.541	403.6	0.014	0.73	0.011	0.76	0.008	0.80
ATP	507	0.633	387.5	0.018	0.72	0.014	0.75	0.010	0.79
IGF-1	7600	1.540	150	0.092	0.65	0.071	0.68	0.050	0.73
PTH	9500	1.623	134.6	0.101	0.64	0.078	0.68	0.055	0.73
sclerostin	24000	2.210	98.8	0.173	0.59	0.134	0.64	0.095	0.69
sRANKL	24000	2.210	98.8	0.173	0.59	0.134	0.64	0.095	0.69
TGF-β	25000	2.241	97.5	0.177	0.59	0.137	0.63	0.097	0.69
TRAP	35000	2.506	87.1	0.215	0.57	0.166	0.62	0.117	0.67

OPG	60000	3.000	72.8	0.293	0.54	0.226	0.59	0.159	0.64
DMP-1	100,000	3.557	61.4	0.392	0.50	0.303	0.55	0.215	0.61
OPG	120,000	3.779	57.8	0.435	0.49	0.336	0.54	0.238	0.60
Romosozumab	146,000	4.035	54.1	0.486	0.48	0.375	0.52	0.265	0.59

Note: The PCM fiber radius = 2 nm (size of perlecan core protein, major component of the PCM fibers) 48 and the fiber volume fraction of the PCM in the nulliparous LCS = 0.061 34 . Reflection coefficient was calculated based on the sieving model by Wang et al. 38 and the reduced diffusivity was predicted using the Curry-Michel model 57 .

4. Discussion

The motivation behind this multiscale computational study was to understand how lactation-induced microstructural changes affect the local biophysical and biochemical environment of osteocytes, and the potential consequences on the metabolism and mechanobiology of the maternal skeleton. Robust peri-lacunar remodeling has been demonstrated convincingly in lactating bone, which shows higher sensitivity to mechanical loading ¹⁵ and more resistance to postmenopausal bone loss later in life ¹⁶. These intriguing observations prompted us to ask whether lactation alters loading-induced fluid flow around osteocytes and increases their sensitivity to mechanical loading ¹⁰. The multiscale modeling presented herein allowed us to quantify and compare various flow-mediated stimulations on the mechanosensing complex of the osteocyte, including the cell membrane, pericellular tethering fibers, and primary cilium. The effects of lactation on convection and diffusion of signaling molecules and nutrients relevant to osteocyte function were also investigated, using models incorporating key LCS features of lactating and nulliparous murine tibiae.

This study revealed three major findings. First, for a given loading magnitude, loading frequency and two structural parameters, LCS porosity and PCM density, were found to be major determinants of fluid flow and solute transport in bone, all of which osteocytes depend on for

mechanosensing, cell-cell signaling, and metabolism. Second, while lactation-induced LCS expansion and PCM thinning were shown to promote solute transport and bending of the primary cilia under 0.5 Hz loading, the fluid shear and/or drag force were significantly decreased on the cell membrane, demonstrating lactation-induced deficits in osteocyte mechanosensing under low-frequency loading. However, increasing the loading frequency to 2 or 4 Hz, which were commonly used to elicit *in vivo* bone formation ^{42, 60, 61}, can counteract these deficits. Remarkably, the countering effects were shown to be more pronounced in the canaliculi of lactating bone with PCM loss (75% *kvf* or 50%*kvf* vs. 100% *kvf*). Third, loading at a higher frequency and sparser PCM synergistically promote solute transport in the LCS. Overall, these findings demonstrate that the biophysical and biochemical changes caused by lactation could serve as feedback control signals, and this self-regulation loop may contribute, at least partially, to the rapid recovery of the maternal skeleton by enhanced solute transport and increased sensitivity to loading associated with fast locomotion.

These simulations align with our experimental study ¹⁵, in which we compared bone formation rates among virgin, pregnant, lactating, and post-weaning rats subjected to 2-week tibial loading at 1500 με and 2 Hz. We discovered that the fold change of periosteal bone formation rate (loaded vs. non-loaded tibiae) was significantly greater in lactating rats (~25 fold) than in the other three groups (~5 to 10). In mice and rats, the ultimate load and stiffness of the whole bone and the intrinsic modulus of bone tissue were fully recovered one to three weeks post-weaning to the levels of nulliparous controls as shown by three-point bending ^{62,63} and microindentation tests ¹². Thus, our experimental and modeling results are consistent with previous observations that lactation imparts no adverse fracture risk for the maternal skeleton and even provide some long-term

benefits in bone health in human and animals ^{18, 64}. The history of reproduction and lactation may prime the osteocytes to better respond to anabolic mechanical loading.

417

418

419

420

421

422

423

424

425

426

427

428

429

430

431

432

433

434

435

436

437

438

In addition, the present multiscale model advances the understanding of load-induced fluid and solute transport during lactation. The LCS enlargement and potential PCM thinning during lactation lead to higher hydraulic permeability in bone. While one may expect increased fluid flow as a result, our calculations instead showed decreased fluid velocity in the case of slower loading rate (e.g., 0.5 Hz). This counter-intuitive result is due to the interplay between loading frequency, fluid pressurization/relaxation, and hydraulic permeability. In a porous medium with higher permeability, fluid relaxes relatively faster, and thus pressure build up does not occur. With the widening of fluid gap in the canaliculi and lacuna in lactating bone, fluid velocity, fluid shear, and fluid drag become lessened even more due to the principle of continuity of fluids. In contrast, when loading frequency is increased, the inability of fluid to quickly relax in between loading cycles causes fluid pressure to accumulate, and as a result higher fluid velocity and greater fluid forces are generated. This frequency-dependent enhancement is more pronounced at the cell process than the cell body, and the former has been found to be a more sensitive site for osteocytes to detect mechanical stimulation 65. Consistently, the expansion of the lacunae leads to higher bending moment on primary cilia, which could also activate osteocytes ³². Furthermore, lactation enhances solute transport owing to the expansion of the transport conduits and lower sieving effects. We found faster diffusion, reduced hindrance in convection, and elevated total volumetric influx of nutrients and signaling molecules in lactating bone, regardless of molecule size or loading rate. Solute transport is essential for osteocyte survival (nutrient supply and waste removal) and osteocyte function (cell-cell signaling) ²⁹. Taken together, lactation-induced structural changes alter the biophysical and biochemical environment of osteocytes in ways that could favor maternal bone's post-weaning recovery, metabolism and mechanosensing.

The modeling approach employed in this study has several noteworthy strengths. The multiscale modeling framework takes several interconnected structural levels into consideration, spanning from whole bone (~15 x 2 mm size), to porous bone tissue (~0.2mm cortex), to individual lacunar and canalicular fluid conduits (~0.1-1 µm fluid gap), and to the pericellular matrix fibers (~10 nm fiber spacing). Adopting the theoretical framework pioneered by Weinbaum *et al.* ^{27, 35} and further developed by us and others ^{34, 38, 40, 43, 48}, we established two model scenarios for nulliparous and lactating bones where the poroelastic properties of bone tissue, hydraulic permeability, and sieving property of the pericellular matrix surrounding the osteocytes are based on available experimental measurements. In particular, the discovery of perlecan as a major component of the pericellular matrix tethering element ⁴⁹, the subsequent measurement of the size of perlecan ⁴⁸, and the fiber volume fraction of the PCM density in young and aged mice ³⁴ greatly improve the capability of predicting flow-mediated stimulations and solute transport characteristics.

Our study also has some limitations. The model of lactating bone incorporates not only the enlargement of the lacunae and canaliculi ^{8, 12}, but also potential degradation of the PCM fibers, a reasonable extrapolation based on the capability of the osteocytes in matrix lysis ^{8, 9, 11-14}. The PCM density in lactation bone has not been quantified experimentally and thus was parametrically varied and reduced than that of the nulliparous control. However, the actual value remains to be determined experimentally. In addition, the murine tibial midshaft was simplified as a hollow cylinder. A more complex 3D finite element modeling based on bone architecture ⁶⁶ could improve the model predictions. To simplify the modeling approach, isotropic mechanical properties and

permeability of midshaft cortex were assumed 40 due to the presence of few vascular pores. The contribution of vascular pores to bone fluid flow, especially their role of a low-pressured fluid reservoir, has been demonstrated in normal or osteoporotic bone ^{67, 68}. Furthermore, we chose a region of interest below the periosteum at the medial surface to be consistent with previous studies that provided key measurements that were subsequently used in the model ^{34, 38, 40, 43, 48}. At this location, circumferential flow is dominant, leading to more simplified calculations ⁴⁰. Although the numerical results may differ at other anatomical locations, we expect to reach the same general conclusions regarding the comparisons between the lactating vs. nulliparous bone in the fluid flow and solute transport. We also simplified canaliculi to resemble straight channels, based on our measurements of their tortuosity (~1.2) at the midshaft lamellar cortex for both nulliparous and lactating rats (Supplementary Materials, Figure 2S). Canalicular tortuosity is predicted to reduce bone permeability and flow velocity as demonstrated by Lemaire ⁶⁹. Last but not least, the model outputs quantify the changes in the mechanical environment around osteocytes, however the downstream cellular responses of osteocytes in lactating skeleton (such as mechanotransduction) also depend on additional factors including hormonal changes, which are beyond the scope of this study.

461

462

463

464

465

466

467

468

469

470

471

472

473

474

475

476

477

478

479

480

481

482

In summary, we investigated how structural changes in LCS and PCM during lactation alter the local biophysical and biochemical cues for osteocytes, which may influence adaptation of maternal bone to physiological load bearing and weight-bearing exercise postpartum and drive its post-weaning recovery. We found that variations of loading frequency, LCS porosity and PCM affect the local fluid environment and transport around osteocytes. In particular, we identified deficits in flow-mediated stimulation of osteocytes in lactating bone under 0.5 Hz loading.

Remarkably, loading at a higher frequency (2 or 4 Hz) can overcome most deficits and enhance transport in lactating bone. These results support the roles of osteocytes and their local fluid environment in the homeostasis of female skeleton and its adaptation to mechanical loading.

Author Statements:

X. Lai: Conceptualization; Methodology; Software, Data Curation; Formal analysis; Writing-Original Draft, Review & Editing; Visualization; Funding acquisition. R. Chung: Formal analysis; Writing-Review & Editing; Y. Li: Data Curation; Formal analysis; Review & Editing. X.S. Liu: Conceptualization; Formal analysis; Writing-Review & Editing; L. Wang: Conceptualization; Methodology; Formal analysis; Writing-Original Draft, Review & Editing

Acknowledgements: this study was supported by the National Natural Science Foundation of China (Grant No. 31800783 to X Lai), the Fundamental Research Funds for the Central Universities to X Lai, National Institute of Health (AR076906 to R Chung; AR071718 to XS Liu, AR054385 to LW), and National Science Foundation (Award #1653216 to XS Liu).

497 **References:**

- 498 1. Rigal A and Vignal W, *Recherches experimentales sur la formation du cal et sur les modifications des tissue* 499 *dans les pseudoarthroses.* Arch Physiol Ser II 1881. **8**: p. 419–58.
- 500 2. Recklinghausen F, *Untersurchungen uber Rachitis and Osteomalacia*. 1910: Jena: Gustav Fischer.
- Heller-Steinberg M, *Ground substance, bone salts, and cellular activity in bone formation and destruction.*Am J Anat, 1951. **89**(3): p. 347-79.
- Belanger LF, Osteocytic osteolysis. Calcif Tissue Res, 1969. **4**(1): p. 1-12.
- 504 5. Rasmussen P, *Calcium deficiency, pregnancy, and lactation in rats. Microscopic and microradiographic observations on bones.* Calcif Tissue Res, 1977. **23**(1): p. 95-102.
- 506 6. Parfitt AM, *The cellular basis of bone turnover and bone loss: a rebuttal of the osteocytic resorption--bone flow theory.* Clin Orthop Relat Res, 1977(127): p. 236-47.
- 508 7. Bonewald LF, *The amazing osteocyte*. J Bone Miner Res, 2011. **26**(2): p. 229-38.
- 509 8. Qing H, Ardeshirpour L, Pajevic PD, Dusevich V, Jahn K, Kato S, Wysolmerski J, and B. LF., *Demonstration*510 of osteocytic perilacunar/canalicular remodeling in mice during lactation. J Bone Miner Res, 2012. **27**(5): p.
 511 1018-29.
- 512 9. Wysolmerski JJ, *Osteocytic osteolysis: time for a second look?* Bonekey Rep, 2012. **1**: p. 229.
- 513 10. Liu XS, Wang L, de Bakker CMJ, and Lai X, *Mechanical regulation of the maternal skeleton during* 514 reproduction and lactation. Curr Osteoporos Rep, 2019. **17**(6): p. 375-386.
- Jahn K, Kelkar S, Zhao H, Xie Y, Tiede-Lewis LM, Dusevich V, and B.L. Dallas SL, *Osteocytes acidify their microenvironment in response to PTHrP in vitro and in lactating mice in vivo.* J Bone Miner Res, 2017. **32**(8): p. 1761-1772.
- Kaya S, Basta-Pljakic J, Seref-Ferlengez Z, Majeska RJ, Cardoso L, Bromage TG, and e. al., *Lactation-induced changes in the volume of osteocyte lacunar-canalicular space alter mechanical properties in cortical bone* bone Miner Res, 2017. 32(4): p. 688-697.
- 521 13. Wysolmerski JJ, *Osteocytes remove and replace perilacunar mineral during reproductive cycles.* Bone, 2013. 54(2): p. 230-6.
- Lotinun S, Ishihara Y, Nagano K, Kiviranta R, Carpentier VT, Neff L, Parkman V, Ide N, and D. Hu, Dann, P., Brooks, D., Bouxsein, M. L., Wysolmerski, J., Gori, F., Baron, R., *Cathepsin K-deficient osteocytes prevent*
- 525 *lactation-induced bone loss and parathyroid hormone suppression.* J Clin Invest, 2019. **129**(8): p. 3058-526 3071.
- Li Y, de Bakker CMJ, Zhao H, Parajuli A, Tseng WJ, Pei S, Tan M, Chung R, Wang L, and L. XS, *Maternal Bone Adaptation to Mechanical Loading during Pregnancy, Lactation, and Post-Weaning Recovery.* BONE,
 2021. Submitted to Mechanobiology Special Issue.
- de Bakker CM, Li Y, Zhao H, Leavitt L, Tseng WJ, Lin T, Tong W, Qin L, and Liu XS, *Structural adaptations in the rat tibia bone induced by pregnancy and lactation confer protective effects against future estrogen deficiency.* J Bone Miner Res, 2018. **33**(12): p. 2165-2176.
- 533 17. Kovacs CS, *Maternal mineral and bone metabolism during pregnancy, lactation, and post-weaning recovery.* Physiol Rev, 2016. **96**(2): p. 449-547.
- de Bakker CM, Altman-Singles AR, Li Y, Tseng WJ, Li C, and Liu XS, *Adaptations in the microarchitecture*and load distribution of maternal cortical and trabecular bone in response to multiple reproductive cycles
 in rats. J Bone Miner Res, 2017. **32**(5): p. 1014-1026.
- 538 19. Laskey MA, Price RI, Khoo BC, and Prentice A, *Proximal femur structural geometry changes during and following lactation.* Bone, 2011. **48**(4): p. 755-9.

- 540 20. Bjornerem A, Ghasem-Zadeh A, Wang X, Bui M, Walker SP, Zebaze R, and Seeman E, *Irreversible deterioration of cortical and trabecular microstructure associated with breastfeeding.* J Bone Miner Res, 2017. **32**(4): p. 681-687.
- Liu XS, Ardeshirpour L, VanHouten JN, Shane E, and Wysolmerski JJ, *Site-specific changes in bone microarchitecture, mineralization, and stiffness during lactation and after weaning in mice.* J Bone Miner Res, 2012. **27**(4): p. 865-75.
- Hellmeyer L, Hahn B, Fischer C, Hars O, Boekhoff J, Maier J, and H. P., *Quantitative ultrasonometry during* pregnancy and lactation: a longitudinal study. Osteoporos Int, 2015. **26**(3): p. 1147-54.
- Tsourdi E, Jahn K, Rauner M, Busse B, and Bonewald LF, *Physiological and pathological osteocytic osteolysis.*J Musculoskelet Neuronal Interact, 2018. **18**(3): p. 292-303.
- Tang SY, Herber RP, Ho SP, and Alliston T, *Matrix metalloproteinase-13 is required for osteocytic perilacunar remodeling and maintains bone fracture resistance.* J Bone Miner Res, 2012. **27**(9): p. 1936-50.
- Yee CS, Schurman CA, White CR, and Alliston T, *Investigating osteocytic perilacunar/canalicular remodeling*.
 Curr Osteoporos Rep, 2019. 17(4): p. 157-168.
- 554 26. Schaffler, M.B., W.Y. Cheung, R. Majeska, and O. Kennedy, *Osteocytes: master orchestrators of bone.* Calcif Tissue Int, 2014. **94**(1): p. 5-24.
- Weinbaum S, Cowin SC, and Zeng Y, *A model for the excitation of osteocytes by mechanical loading-induced bone fluid shear stresses.* J Biomech, 1994. **27**(3): p. 339-60.
- 558 28. Burger, E.H., J. Klein-Nulend, A. van der Plas, and P.J. Nijweide, *Function of osteocytes in bone--their role* 559 *in mechanotransduction.* J Nutr, 1995. **125**(7 Suppl): p. 2020S-2023S.
- 560 29. Wang L, *Solute transport in the bone lacunar-canalicular system (LCS).* Curr Osteoporos Rep, 2018. **16**(1): p. 32-41.
- 562 30. Burger, E.H. and J. Klein-Nulend, *Mechanotransduction in bone--role of the lacuno-canalicular network.*563 FASEB J, 1999. **13 Suppl**: p. S101-12.
- 564 31. Knothe Tate, M.L., "Whither flows the fluid in bone?" An osteocyte's perspective. J Biomech, 2003. **36**(10): p. 1409-24.
- Malone AM, Anderson CT, Tummala P, Kwon RY, Johnston TR, Stearns T, and J. CR., *Primary cilia mediate mechanosensing in bone cells by a calcium-independent mechanism.* Proc Natl Acad Sci U S A, 2007. **104**(33): p. 13325-30.
- 569 33. Schaffler MB and Kennedy OD, Osteocyte signaling in bone. Curr Osteoporos Rep, 2012. 10(2): p. 118-25.
- Wang B, Lai X, Price C, Thompson WR, Li W, Quabili TR, Tseng WJ, and X.S. Liu, Zhang, H., Pan, J., Kirn-Safran, C. B., Farach-Carson, M. C., Wang, L., *Perlecan-containing pericellular matrix regulates solute transport and mechanosensing within the osteocyte lacunar-canalicular system.* J Bone Miner Res, 2014.
- **29**(4): p. 878-91.
- 574 35. You L, Cowin SC, Schaffler MB, and Weinbaum S, *A model for strain amplification in the actin cytoskeleton*575 of osteocytes due to fluid drag on pericellular matrix. J Biomech, 2001. **34**(11): p. 1375-86.
- 576 36. Fritton SP and Weinbaum S, *Fluid and solute transport in bone: flow-induced mechanotransduction.* Annu Rev Fluid Mech, 2009. **41**: p. 347-374.
- 578 37. Jing D, Baik AD, Lu XL, Zhou B, Lai X, Wang L, Luo E, and G. XE., *In situ intracellular calcium oscillations in osteocytes in intact mouse long bones under dynamic mechanical loading.* FASEB J, 2014. **28**(4): p. 1582-580 92.
- Wang B, Zhou X, Price C, Li W, Pan J, and Wang L, *Quantifying load-induced solute transport and solute-matrix interactions within the osteocyte lacunar-canalicular system.* J Bone Miner Res, 2013. **28**(5).
- 583 39. Li W, You L, Schaffler MB, and Wang L, The dependency of solute diffusion on molecular weight and shape

- *in intact bone.* Bone, 2009. **45**(5): p. 1017-23.
- Zhou X, Novotny JE, and Wang L, *Modeling fluorescence recovery after photobleaching in loaded bone:*potential applications in measuring fluid and solute transport in the osteocytic lacunar-canalicular system.
- 587 Ann Biomed Eng, 2008. **36**(12): p. 1961-77.
- Lynch ME, Main RP, Xu Q, Schmicker TL, Schaffler MB, Wright TM, and v.d.M. MC., *Tibial compression is anabolic in the adult mouse skeleton despite reduced responsiveness with aging.* Bone, 2011. **49**(3): p. 439-46.
- Pei S, Parthasarathy S, Parajuli A, Martinez J, Lv M, Jiang S, Wu D, Wei S, and F.-C. Lu XL, M. C., Kirn-Safran,
 C. B., Wang, L., *Perlecan/Hspg2 deficiency impairs bone's calcium signaling and associated transcriptome in response to mechanical loading.* Bone, 2020. 131: p. 115078.
- 594 43. Price C, Zhou X, Li W, and Wang L, *Real-time measurement of solute transport within the lacunar-canalicular system of mechanically loaded bone: direct evidence for load-induced fluid flow.* J Bone Miner Res, 2011. **26**(2): p. 277-85.
- Wang L, Wang Y, Han Y, Henderson SC, Majeska RJ, Weinbaum S, and S. MB., *In situ measurement of solute transport in the bone lacunar-canalicular system.* Proc Natl Acad Sci U S A, 2005. 102(33): p. 11911-6.
- 600 45. Cowin SC, Weinbaum S, and Zeng Y, *A case for bone canaliculi as the anatomical site of strain generated*601 *potentials.* J Biomech, 1995. **28**(11): p. 1281-97.
- 602 46. Lai X, Price C, and Wang L, *Osteocyte lacunae and canaliculi in cortical and trabecular bones*, in 603 *Orthopaedic Research Society*. 2012.
- Parajuli, A., C. Liu, W. Li, X. Gu, X. Lai, S. Pei, C. Price, L. You, X.L. Lu, and L. Wang, *Bone's responses to mechanical loading are impaired in type 1 diabetes.* Bone, 2015. **81**: p. 152-160.
- Wijeratne SS, Martinez JR, Grindel BJ, Frey EW, Li J, Wang L, Farach-Carson MC, and K. CH., *Single molecule force measurements of perlecan/HSPG2: A key component of the osteocyte pericellular matrix.* Matrix Biol, 2016. **50**: p. 27-38.
- Thompson WR, Modla S, Grindel BJ, Czymmek KJ, Kirn-Safran CB, Wang L, Duncan RL, and F.-C. MC., Perlecan/Hspg2 deficiency alters the pericellular space of the lacunocanalicular system surrounding osteocytic processes in cortical bone. J Bone Miner Res, 2011. **26**(3): p. 618-29.
- Krempien B, Friedrich E, and Ritz E, *Effect of PTH on osteocyte ultrastructure*. Adv Exp Med Biol, 1978. **103**: p. 437-50.
- Tazawa K, Hoshi K, Kawamoto S, Tanaka M, Ejiri S, and Ozawa H, *Osteocytic osteolysis observed in rats to which parathyroid hormone was continuously administered.* J Bone Miner Metab, 2004. **22**(6): p. 524-9.
- Sun S, Fisher RL, Bowser SS, Pentecost BT, and Sui H, *Three-dimensional architecture of epithelial primary cilia.* Proc Natl Acad Sci U S A, 2019. **116**(19): p. 9370-9379.
- Lai X, Price C, Modla S, Thompson WR, Caplan J, Kirn-Safran CB, and W. L., *The dependences of osteocyte network on bone compartment, age, and disease.* Bone Res, 2015. **3**: p. 72-82.
- Venier P, Maggs AC, Carlier MF, and Pantaloni D, *Analysis of microtubule rigidity using hydrodynamic flow and thermal fluctuations.* J Biol Chem, 1994. **269**(18): p. 13353-60.
- Belanger LF, Jarry L, and Uhthoff HK, *Osteocytic osteolysis in Paget's disease.* Rev Can Biol, 1968. **27**(1): p. 37-44.
- 624 56. Bonucci E and Gherardi G, *Osteocyte ultrastructure in renal osteodystrophy.* Virchows Arch A Pathol Anat Histol, 1977. **373**(3): p. 213-31.
- 626 57. Curry FE and Michel CC, *A fiber matrix model of capillary permeability.* Microvasc Res, 1980. **20**(1): p. 96-627 9.

- Polson A, *Some aspects of diffusion in solution and a definition of a colloidal particle.* J. Phys. Colloid Chem., 1950. **54**: p. 649–652.
- Tyn MT and Gusek TW, *Prediction of diffusion coefficients of proteins*. Biotechnol Bioeng, 1990. **35**(4): p. 327-38.
- 632 60. Fritton JC, Myers ER, Wright TM, and van der Meulen MC, *Loading induces site-specific increases in mineral*633 *content assessed by microcomputed tomography of the mouse tibia.* Bone, 2005. **36**(6): p. 1030-8.
- Sun D, Brodt MD, Zannit HM, Holguin N, and Silva MJ, *Evaluation of loading parameters for murine axial tibial loading: Stimulating cortical bone formation while reducing loading duration.* J Orthop Res, 2018. **36**(2): p. 682-691.
- 637 62. Vajda EG, Bowman BM, and Miller SC, *Cancellous and cortical bone mechanical properties and tissue*638 *dynamics during pregnancy, lactation, and postlactation in the rat.* Biol Reprod, 2001. **65**(3): p. 689-95.
- 63. Gillies BR, Ryan BA, Tonkin BA, Poulton IJ, Ma Y, Kirby BJ, St-Arnaud R, Sims NA, and K. CS., *Absence of calcitriol causes increased lactational bone loss and lower milk calcium but does not impair post-lactation bone recovery in cyp27b1 null mice.* J Bone Miner Res, 2018. **33**(1): p. 16-26.
- 642 64. Wiklund PK, Xu L, Wang Q, Mikkola T, Lyytikainen A, Volgyi E, E. Munukka, and A. Cheng S. M., M., 643 Keinanen-Kiukaanniemi, S., Cheng, S., *Lactation is associated with greater maternal bone size and bone* 644 *strength later in life.* Osteoporos Int, 2012. **23**(7): p. 1939-45.
- 65. Burra S, Nicolella DP, Francis WL, Freitas CJ, Mueschke NJ, Poole K, and Jiang JX, *Dendritic processes of osteocytes are mechanotransducers that induce the opening of hemichannels.* Proc Natl Acad Sci U S A, 2010. **107**(31): p. 13648-53.
- 648 66. Fan L, Pei S, Lu XL, and Wang L, *A multiscale 3D finite element analysis of fluid/solute transport in mechanically loaded bone.* Bone Res, 2016. **4**: p. 16032.
- 650 67. Fornells, P., J.M. Garcia-Aznar, and M. Doblare, *A finite element dual porosity approach to model deformation-induced fluid flow in cortical bone.* Ann Biomed Eng, 2007. **35**(10): p. 1687-98.
- 652 68. Gatti, V., E.M. Azoulay, and S.P. Fritton, *Microstructural changes associated with osteoporosis negatively*653 *affect loading-induced fluid flow around osteocytes in cortical bone.* J Biomech, 2018. **66**: p. 127-136.
- 654 69. Lemaire, T., S. Lemonnier, and S. Naili, *On the paradoxical determinations of the lacuno-canalicular permeability of bone.* Biomech Model Mechanobiol, 2012. **11**(7): p. 933-46.

Supplementary Materials

659

658

1. Theory and Calculations

660 661

662

676

677

678

679

680

- 1.1 The LCS permeability, fluid pore pressure, pressure gradient, shear stress, shear force and
- 663 *drag force*
- The hydraulic permeability of a single canaliculus k_p is given by

665
$$\frac{1}{k_p} = \frac{2}{3k_{p1}} + \frac{1}{3k_{p2}},\tag{A1}$$

where k_{p1} is the Darcy permeability of the transverse fibers including the core proteins and k_{p2} the axial fibers. The expression for k_{p1} is given in Weinbaum *et al.* ¹ as:

$$k_{p1} = 0.0572a_0^2 (\Delta / a_0)^{2.377}, \tag{A2}$$

The expression for k_{p2} is given in Cowin *et al.* ² as:

$$k_{p2} = 0.147 a_0^2 (\Delta / a_0)^{2.285}, \tag{A3}$$

- where a_0 is the radius of the pericellular fibers and Δ is the edge-to-edge spacing of the fibers in the pericellular matrix and related to the volume fraction of the PCM as $kvf = \frac{\pi r_f^2}{(\Lambda + 2r_e)^2}$.
- The tissue level permeability is estimated from the anatomical features of the LCS as in

 Weinbaum *et al.* ¹:

675
$$k = \frac{2\pi N a^4 q^3}{6\gamma^3 d^2} \left\{ A_1 [I_1(\gamma/q) - qI_1(\gamma)] + B_1 [qK_1(\gamma) - K_1(\gamma/q)] + \frac{\gamma(q^2 - 1)}{2q} \right\}, \quad (A4)$$

where a is the radius of the osteocyte process, q is the ratio of the radius of the canaliculus (b) to the radius of the osteocytic process (a), d is the average spacing between two lacunae, N is the total number of canaliculi emanating from one lacuna, γ is a dimensionless length ratio between the canalicular radius and its associated boundary layer thickness, which is approximated to be the square root of the permeability of a single canaliculus ($\gamma = b/\sqrt{k_p}$). A_1 and B_1 are defined as

681
$$A_1 = \frac{K_0(\gamma) - K_0(\gamma/q)}{I_0(\gamma/q)K_0(\gamma) - I_0(\gamma)K_0(\gamma/q)}$$
 (A5)

$$B_1 = \frac{I_0(\gamma/q) - I_0(\gamma)}{I_0(\gamma/q) K_0(\gamma) - I_0(\gamma) K_0(\gamma/q)}$$
(A6)

- Where I_0 , K_0 , I_1 and K_1 are modified Bessel functions of the first and second kind.
- The characteristic fluid relaxation time, which will be used in the dimensionless Biot equation
- 685 listed below, is defined as:

$$\tau_r = \frac{\mu r_0^2}{k(13.5GP_a)} \tag{A7}$$

- where μ is the viscosity of bone fluid and assumed to be that of sea water ($\mu = 1.06 \times 10^{-3} \text{ kg/ms}$);
- r_o is the radius of the periosteum.
- The intermittent dynamic force is given below:

690
$$f(t) = F\left(-\frac{1}{2} + \frac{1}{2}\cos\frac{\pi t}{t_1}\right), \tag{A8}$$

- Where F is the peak-to-peak force (6 N in our case) and $2t_1$ is the loading period (=1/loading
- frequency, 2 s for 0.5 Hz, 1 s for 2 Hz, and 0.5 s for 4 Hz loading).
- The pore fluid pressure p in the LCS due to the applied loading can be calculated from a
- previously developed equation based on the Biot poroelastic theory ³:

695
$$\frac{\partial^2 p}{\partial r^2} + \frac{1}{r} \frac{\partial p}{\partial r} + \frac{1}{r^2} \frac{\partial^2 p}{\partial \theta^2} - \frac{1}{c} \frac{\partial p}{\partial t} = \frac{B}{3c} \left[\frac{1}{A} + \frac{rL}{I} \sin \theta \right] \frac{df(t)}{dt}, \tag{A9}$$

- Where c is the pore pressure diffusion coefficient ($c = r_o^2/\tau_r$) and B is the Skempton parameter
- 697 indicating the relative compressibility between the fluid and solid phases in bone (B = 0.53).
- Using a set of parameters $[R = r/r_o; \tau = t/\tau_r; T = \omega \tau_r; \omega = \pi/t_1; \text{ and } P = 3pA/(BTF)]$ and
- substituting the expression of loading f(t), the Biot poroelastic equation of the fluid pore pressure
- 700 is rendered dimensionless ³:

701
$$\frac{\partial^2 P}{\partial P^2} + \frac{1}{P} \frac{\partial P}{\partial P} + \frac{1}{P^2} \frac{\partial^2 P}{\partial \theta^2} - \frac{\partial P}{\partial \tau} = -\left[1 + \frac{Lr_0 A}{I} R \sin \theta\right] \times \frac{1}{2} \sin(T\tau) \tag{A10}$$

where R, τ , T, and P are dimensionless radial position, time, frequency, and pressure respectively;

 ω is the principle angular loading frequency; F is the peak force of the dynamic loading; A is the cross-sectional area of the tibial midshaft; r_0 is the exterior radius of the tibial midshaft, L is the offset of the loading force to the center of the bone, I is the moment of inertia of the bone cross-section along the medial-lateral axis 3 .

The boundary conditions are zero pressure at the inner endosteal surface and a leaky outer periosteal surface as in previous models ³:

709
$$P = 0 \text{ at } R = \lambda = r_i/r_o; \ \frac{\partial P}{\partial R} + \eta P = 0 \text{ at } R = 1$$
 (A11)

where η is the coefficient with $\eta = 0$ corresponding to no leakage condition and $\eta \to \infty$ corresponding to free flow condition. In this study, we use no leakage condition ($\eta = 0$).

The analytical solution of dimensionless pressure is derived using complex function and separate variables as follows ³:

714
$$P(R,\theta,\tau) = \operatorname{Im}\left\{\left[\frac{1}{2iT}\left(1 + \frac{Lr_0A}{I}R\sin\theta\right) + C_{01}I_0(\sqrt{iT}R) + D_{01}K_0(\sqrt{iT}R) + C_{01}I_0(\sqrt{iT}R)\right]\right\}$$

$$\left(C_{11}I_1(\sqrt{iT}R) + D_{11}K_1(\sqrt{iT}R)\right)\sin\theta\right]e^{iT\tau}\right\}$$
(A12)

716 where

717
$$C_{01} = \frac{1}{2iT} \frac{\sqrt{iT} K_1(\sqrt{iT}) - \eta [K_0(\sqrt{iT}) - K_0(\lambda\sqrt{iT})]}{I_0(\lambda\sqrt{iT})[\sqrt{iT} K_1(\sqrt{iT}) - \eta K_0(\sqrt{iT})] + K_0(\lambda\sqrt{iT})[\sqrt{iT} I_1(\sqrt{iT}) + \eta I_0(\sqrt{iT})]}$$
(A13)

718
$$D_{01} = \frac{1}{2iT} \frac{\sqrt{iT}I_{1}(\sqrt{iT}) + \eta[I_{0}(\sqrt{iT}) - I_{0}(\lambda\sqrt{iT})]}{I_{0}(\lambda\sqrt{iT})[\sqrt{iT}K_{1}(\sqrt{iT}) - \eta K_{0}(\sqrt{iT})] + K_{0}(\lambda\sqrt{iT})[\sqrt{iT}I_{1}(\sqrt{iT}) + \eta I_{0}(\sqrt{iT})]}$$
(A14)

719
$$C_{11} = -\frac{Lr_0 A}{2iIT} \frac{\lambda \left[\sqrt{iT} K_0(\sqrt{iT}) + (1-\eta) K_1(\sqrt{iT})\right] + (1+\eta) K_1(\lambda \sqrt{iT})}{I_1(\lambda \sqrt{iT}) \left[\sqrt{iT} K_0(\sqrt{iT}) + (1-\eta) K_1(\sqrt{iT})\right] + \left[\sqrt{iT} I_0(\sqrt{iT}) - (1-\eta) I_1(\sqrt{iT})\right] K_1(\lambda \sqrt{iT})}$$

720 (A15)

721
$$D_{11} = -\frac{Lr_0 A}{2iIT} \frac{\lambda [\sqrt{iT}I_0(\sqrt{iT}) - (1-\eta)I_1(\sqrt{iT})] - (1+\eta)I_1(\lambda\sqrt{iT})}{I_1(\lambda\sqrt{iT})[\sqrt{iT}K_0(\sqrt{iT}) + (1-\eta)K_1(\sqrt{iT})] + [\sqrt{iT}I_0(\sqrt{iT}) - (1-\eta)I_1(\sqrt{iT})]K_1(\lambda\sqrt{iT})}$$
(A16)

The gradients of the dimensionless pressure in the radial and circumferential directions are obtained:

724
$$\frac{\partial P}{\partial R} = \operatorname{Im} \left\{ \left[\frac{Lr_0 A}{2iIT} \sin \theta + C_{01} \sqrt{iT} I_1 \left(\sqrt{iT} R \right) - D_{01} \sqrt{iT} K_1 \left(\sqrt{iT} R \right) + \left(C_{11} \sqrt{iT} I_0 \left(\sqrt{iT} R \right) + C_{01} \sqrt{$$

725
$$\frac{c_{11}}{R}I_1(\sqrt{iT}R) - D_{11}\sqrt{iT}K_0(\sqrt{iT}R) - \frac{D_{11}}{R}K_1(\sqrt{iT}R)\sin\theta e^{iT\tau}$$
 (A17)

726
$$\frac{\partial P}{\partial \theta} = \operatorname{Im} \left\{ \left[\frac{Lr_0 A}{2iIT} R \cos \theta + \left(C_{11} I_1 \left(\sqrt{iT} R \right) + D_{11} K_1 \left(\sqrt{iT} R \right) \right) \cos \theta \right] e^{iT\tau} \right\}$$
(A18)

The corresponding canalicular fluid velocities in the radial and circumferential directions are derived using Darcy's law:

$$u_r = -\frac{k_P}{\mu} \frac{\partial p}{\partial r} = -\frac{k_P B T F}{3 \mu r_0 A} \frac{\partial P}{\partial R}$$
(A19)

730
$$u_{\theta} = -\frac{k_P}{\mu r} \frac{\partial p}{\partial \theta} = -\frac{k_P B T F}{3\mu r A} \frac{\partial P}{\partial \theta}$$
 (A20)

where p is the fluid pressure, P is the dimensionless pressure, and k_p is the permeability of a single canaliculus (defined in Eq. A1).

The above Darcy fluid velocity represents the mean value of the fluid velocity in the LCS channels. To calculate the shear stress on the cell membrane and the drag force on the transverse PCM fibers, the velocity profile across the fiber-filled canaliculi channel is given by Weinbaum *et al.* ¹ as:

738
$$u = \frac{k_p}{\mu} \frac{\partial p}{\partial y} \left[A_1 I_0 \left(\gamma \frac{\rho}{b} \right) + B_1 K_0 \left(\gamma \frac{\rho}{b} \right) - 1 \right]$$
 (A21)

where the y coordinate is along the long axis of the canaliculus and ρ coordinate is the radial direction; b is the radius of the canalicular wall, γ is a dimensionless length ratio between the canalicular radius and its associated boundary layer thickness, which is approximated to be the square root of the permeability of a single canaliculus ($\gamma = b/\sqrt{k_p}$). A_1 and B_1 are defined in Eqs. A5 and A6. I_0 and K_0 are modified Bessel functions of the first kind.

The shear stresses acting at the inner surface of the annular region is obtained from the gradient of the velocity profile ¹:

746
$$s(a) = \mu \frac{\partial u}{\partial \rho}(a) = \frac{b}{\gamma} \frac{\partial p}{\partial y} [A_1 I_1(\gamma/q) - B_1 K_1(\gamma/q)]$$
 (A22)

where a is the radius of the osteocyte process and q = b/a.

The integrated shear force f_s on the entire cell process membrane is obtained from the shear stress ⁴:

750
$$f_{s} = 2\pi a ls(a) = 2\pi a l\left(\mu \frac{\partial u}{\partial \rho}\right) = 2\pi a l\left(\frac{b}{\gamma}\right) \frac{\partial p}{\partial y} \left[A_{1} I_{1}\left(\frac{\gamma}{q}\right) - B_{1} K_{1}\left(\frac{\gamma}{q}\right)\right] \tag{A23}$$

where I_1 and K_1 are modified Bessel functions of the second kind; l is the unit length (= 1 μ m in this study).

The total drag force exerted on the tethering fibers can be obtained by integrating the distributed force over the fluid annulus ⁴:

755
$$f_{d} = 2\pi \left[\int_{a}^{b} \rho \left(\frac{\mu}{k_{p}} u \right) d\rho \right] l$$
756
$$= 2\pi l \frac{\partial p}{\partial y} \left\{ \frac{b^{2}}{\gamma} \left[A_{1} I_{1}(\gamma) - B_{1} K_{1}(\gamma) \right] - \frac{b^{2}}{\gamma q} \left[A_{1} I_{1} \left(\frac{\gamma}{q} \right) - B_{1} K_{1} \left(\frac{\gamma}{q} \right) \right] - \frac{b^{2} - a^{2}}{2} \right\}$$
(A24)

In the lacuna to which multiple canaliculi channels are connected, the Darcy's fluid velocity is calculated based on fluid continuity and the spatial profile is obtained by fitting the flow pattern as described in Eq. A21 so that the average fluid velocity equals the Darcy velocity. The fluid shear stress and fluid drag are calculated similarly as in Eqs. A23 and A24.

1.2. Calculation of the bending moment on the primary cilium

The bending moment of the protruded primary cilium was calculated as below. The lacunar fluid space is simplified as an annulus along the major direction of the lacuna, where the inner surface is the osteocyte cell body of radius a (\sim cell body minor radius) and the outer surface is the lacunar wall of radius b (\sim minor radius of the lacuna).

The 2D planar drag force per length acting on a primary cilium, treated as a cylindrical rod in low Reynolds number Stokes flow is given by Venier *et al.* ⁵ as:

768
$$f(h) = \frac{4\pi\mu V(h)}{\ln(l_n/2d)}$$
 (B1)

in which μ is the fluid viscosity, V(h) is the fluid velocity in the lacunar fluid gap, d is the diameter and l_p is the length of the primary cilium. The primary cilium length is set as 2μ m and diameter 200 nm from literature 6,7 .

The concentrated force (F) on the primary cilium calculated through integration of the distributed force f(r) from osteocyte body membrane to lacunar wall:

$$F = \int_{a}^{b} f(r)dr = \frac{4\pi\mu}{\ln(l_n/2d)} \int_{a}^{b} V(r)dr = \frac{4\pi k_p}{\ln(l_n/2d)} \frac{\partial p}{\partial y} \int_{a}^{b} \left[A_1 I_0 \left(\gamma \frac{r}{b} \right) + B_1 K_0 \left(\gamma \frac{r}{b} \right) - 1 \right] dr$$
 (B2)

where the y coordinate is along the long axis of the lacuna and r coordinate is the radial direction of the fluid annulus; a is the osteocyte body minor radius and b is the lacunar minor radius; γ , A_1 and B_1 are defined before (Eqs. A4-A6); I_0 and K_0 are modified Bessel functions of the first kind.

The distance from concentrated force (*F*) point to cell membrane:

779
$$l = \frac{\int_{a}^{b} rf(r)dr}{\int_{a}^{b} f(r)dr} - a = \frac{a^{4}q^{3}}{k_{p}\gamma^{3}} \frac{\left\{A_{1}[qI_{1}(\gamma) - I_{1}(\gamma/q)] - B_{1}[qK_{1}(\gamma) - K_{1}(\gamma/q)] - \frac{\gamma(q^{2} - 1)}{2q}\right\}}{\int_{a}^{b} \left[A_{1}I_{0}(\gamma\frac{r}{b}) + B_{1}K_{0}(\gamma\frac{r}{b}) - 1\right]dr} - a$$
 (B3)

780 Bending moment on the cell membrane:

781
$$M = \text{Fl} = \frac{4\pi k_p}{\ln(l_p/2d)} \frac{\partial p}{\partial y} \int_a^b \left[A_1 I_0 \left(\gamma \frac{r}{b} \right) + B_1 K_0 \left(\gamma \frac{r}{b} \right) - 1 \right] dr \cdot \left\{ \frac{a^4 q^3}{k_p \gamma^3} \frac{\left\{ A_1 [q I_1(\gamma) - I_1(\gamma/q)] - B_1 [q K_1(\gamma) - K_1(\gamma/q)] - \frac{\gamma(q^2 - 1)}{2q} \right\}}{\int_a^b \left[A_1 I_0 \left(\gamma \frac{r}{b} \right) + B_1 K_0 \left(\gamma \frac{r}{b} \right) - 1 \right] dr} - a \right\}$$
(B4)

where q is the ratio of the lacunar minor radius (b) to the osteocyte body minor radius (a).

In this calculation method, the bending moment is related to the permeability of PCM and pressure gradient in the lacunar annular space. The bending moment is dependent on the fluid gap, regardless of the tilt angle of the cilium.

1.3. Reflection coefficients of solutes

We have recently quantified the relationship between the fiber matrix sieving effect and its ultrastructure, in which the reflection coefficient of the molecules could be derived from the osteocyte pericellular fiber volume fraction ⁸:

$$\sigma = \frac{(\alpha+\beta)^{2} \ln\left(1+\frac{\alpha}{\beta}\right) - \alpha^{2}\beta^{2} - \alpha^{3}\beta - \alpha\beta - \frac{\alpha^{4}}{4} - \frac{\alpha^{2}}{2}}{\beta^{2} - \frac{\beta^{4}}{4} - \ln(\beta) - \frac{3}{4}} + \frac{2}{1-\beta^{4} + 2(1+\beta^{4})\ln\beta} \left\{ \alpha \left(1 + \frac{\beta}{\alpha+\beta}\right) \left[1 + \beta^{2}(\alpha + \beta)^{2}\right] - 2(\alpha+\beta)(1+\beta^{4})\ln(1+\frac{\alpha}{\beta}) \right\}$$
(C1)

Where $\alpha = r_s/R$, $\beta = r_f/R$, r_s is the solute radius, r_f is the fiber radius, and R is the radius of the periodic fluid unit surrounding a fiber, which is related to fiber volume fraction $R = r_f (kvf/3)^{-0.5}$.

2. Parametric study of LCS porosity on flow-mediated stimulations induced by 2 Hz loading (Supplementary Figure 1)

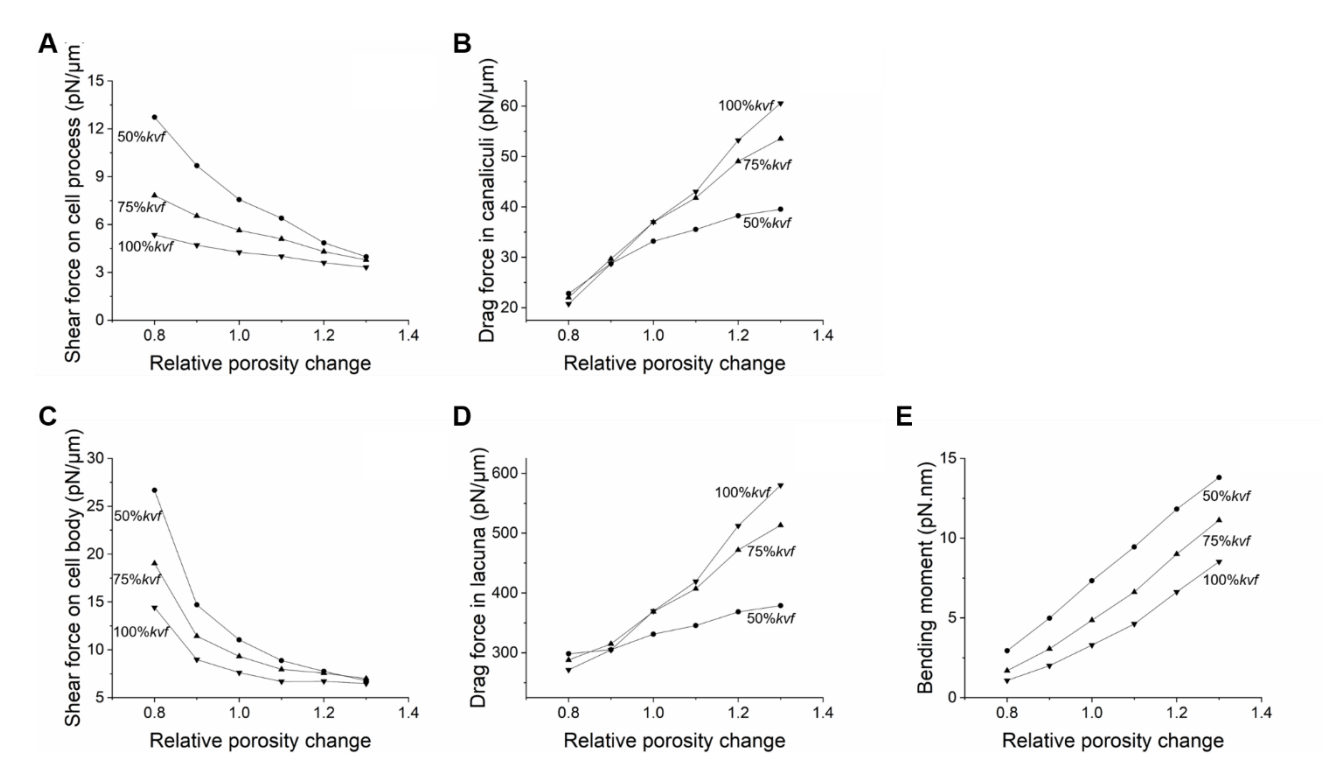


Figure 1S. Parametric study of LCS porosity on flow-mediated stimulations on osteocyte cell processes (in the canaliculus) and cell body (in the lacuna) under loading (3 N, 2 Hz). The reference LCS porosity (=1) is defined as that in the nulliparous bone (detailed structural parameters are listed

in Table 1). The pericellular fiber matrix density is varied at 100%, 75%, and 50% of that in nulliparous bone. The patterns are similar to 3 N and 4 Hz loading as in Figure 3 in the main text: as the LCS porosity increases, shear force decreases, drag force increases, and bending moment of primary cilia increases, while the changing rates for the shear and drag forces vary with the pericellular fiber matrix density.

3. Canalicular tortuosity analysis

Seven-month old female Sprague Dawley rats were assigned to Lactation and age-matched Virgin groups (n=6/group) for canalicular tortuosity analysis. Rats in the Lactation group underwent pregnancy, followed by 2 weeks of lactation, and were euthanized on day 14 of lactation. Ploton silver staining 9 was performed on 8 µm-thick longitudinal paraffin sections of the tibial cortex to visualize the lacunar-canalicular network (Supplemental Figure 2S-AB), and a 133µm*133µm region of the periosteal tibial cortex from both medial and lateral sides located at 1 mm proximal to the distal tibial-fibular junction was selected to measure canalicular tortuosity by ImageJ. Briefly, the lacunar-canalicular network stained by Ploton silver was image processed by local Otsu thresholding, where all lacunae were isolated and removed, thereby resulting in a mask with only canaliculi. The skeleton analysis was further performed to derive branch length and Euclidean distance, and the ratio of branch length to Euclidean distance was interpreted as tortuosity.

Canalicular tortuosity varied from 1.20 to 1.24, and no difference in tortuosity at the periosteal lamellar cortex was observed between Virgin and Lactation rats (Figure 2S-C).

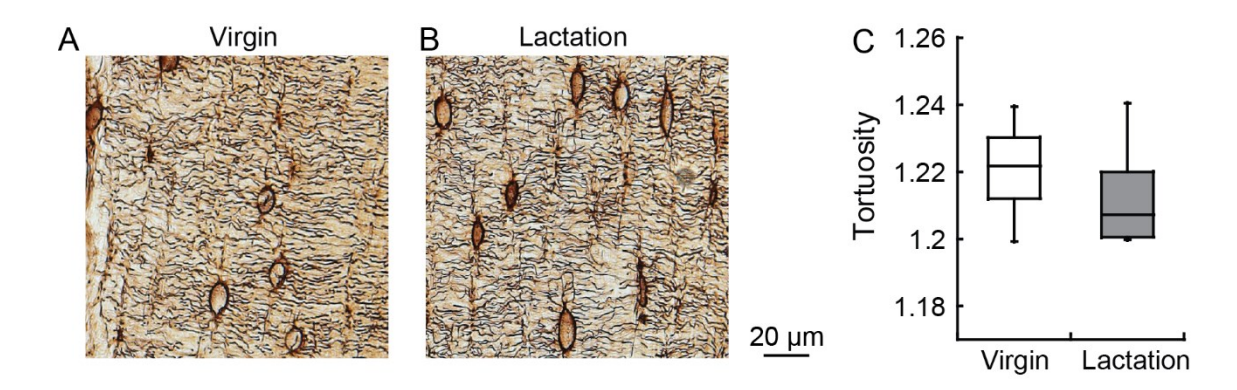


Figure 2S. Measurement of canalicular tortuosity in rat periosteal lamellar cortex. (A, B) Representative images of osteocyte LCS in Virgin and Lactation rats (brown, Ploton Silver staining). (C) Measurement of tortuosity of the canaliculi. No difference was found between Virgin and Lactation rats.

References

824

825

826

827

828

829

830

- Weinbaum S, Cowin SC, and Zeng Y, *A model for the excitation of osteocytes by mechanical loading-induced bone fluid shear stresses.* J Biomech, 1994. **27**(3): p. 339-60.
- Cowin SC, Weinbaum S, and Zeng Y, *A case for bone canaliculi as the anatomical site of strain generated potentials.* J Biomech, 1995. **28**(11): p. 1281-97.
- Zhou X, Novotny JE, and Wang L, Modeling fluorescence recovery after photobleaching in loaded bone:
 potential applications in measuring fluid and solute transport in the osteocytic lacunar-canalicular system.
 Ann Biomed Eng, 2008. 36(12): p. 1961-77.
- You L, Cowin SC, Schaffler MB, and Weinbaum S, *A model for strain amplification in the actin cytoskeleton* of osteocytes due to fluid drag on pericellular matrix. J Biomech, 2001. **34**(11): p. 1375-86.
- Venier P, Maggs AC, Carlier MF, and Pantaloni D, *Analysis of microtubule rigidity using hydrodynamic flow and thermal fluctuations.* J Biol Chem, 1994. **269**(18): p. 13353-60.
- Malone AM, Anderson CT, Tummala P, Kwon RY, Johnston TR, Stearns T, and J. CR., *Primary cilia mediate mechanosensing in bone cells by a calcium-independent mechanism.* Proc Natl Acad Sci U S A, 2007. **104**(33): p. 13325-30.
- Sun S, Fisher RL, Bowser SS, Pentecost BT, and Sui H, *Three-dimensional architecture of epithelial primary cilia.* Proc Natl Acad Sci U S A, 2019. **116**(19): p. 9370-9379.
- 847 8. Wang B, Zhou X, Price C, Li W, Pan J, and Wang L, *Quantifying load-induced solute transport and solute-matrix interactions within the osteocyte lacunar-canalicular system.* J Bone Miner Res, 2013. **28**(5).
- 9. Dole, N.S., C.M. Mazur, C. Acevedo, J.P. Lopez, D.A. Monteiro, T.W. Fowler, B. Gludovatz, F. Walsh, J.N. Regan, S. Messina, D.S. Evans, T.F. Lang, B. Zhang, R.O. Ritchie, K.S. Mohammad, and T. Alliston, *Osteocyte-Intrinsic TGF-beta Signaling Regulates Bone Quality through Perilacunar/Canalicular Remodeling*. Cell Rep, 2017. **21**(9): p. 2585-2596.